NTNU – Trondheim
Norwegian University of
Science and Technology

Connection Between Critical Stress and Hydrogen Content for SDSS under Cathodic Protection

Ola Myklatun Krosness

Materials Science and Engineering
Submission date: June 2014
Supervisor: Roy Johnsen, IPM
Co-supervisor: Afrooz Barnoush, IPM
Jim Stian Olsen, Aker Solutions

Norwegian University of Science and Technology
Department of Engineering Design and Materials

Abstract

In recent years Super Duplex Stainless Steel (SDSS) installed subsea with cathodic protection has failed during service. The failures have been due to Hydrogen Induced Stress Cracking (HISC). The effect from different protection potentials and hydrogen content has been investigated in regarding HISC susceptibility for a Hot Isostatically Pressed (HIP) SDSS according to UNS S32550. Pre-charging has been done in a 2:1 Glycerol – H_3PO_4 electrolyte at 120°C, while in-situ testing has been done in synthetic seawater (3.5% NaCl) at room temperature. Protection potentials have been varied from -1050m$V_{Ag/AgCl}$ to -800m$V_{Ag/AgCl}$. Testing has been done in a small test-jig incorporating a light microscope for crack and microstructural surveillance of the samples. Non-notched and notched samples have been tested. The non-notched samples tested showed to be too ductile for the test-jig, thus only the -1050m$V_{Ag/AgCl}$ sample fractured with a fracture strength of 136±0% of yield strength (YS). There was seen a trend for surface cracks to grow in size for more negative protection potentials. All the notched samples fractured, giving the following results 136±0%, 137.3±1.9%, 144±0%, 148±0% and 140±0% of YS for the -1050m$V_{Ag/AgCl}$, -1000m$V_{Ag/AgCl}$, -950m$V_{Ag/AgCl}$, -900m$V_{Ag/AgCl}$ and -800m$V_{Ag/AgCl}$ samples respectively. A notched sampled tested in air fractured at 161% of YS. The same trend for surface cracks growing in size for more negative potentials, as seen for the non-notched samples, was also seen for the notched samples. All the samples suffered from HISC, with all samples showing high fracture strengths. A hydrogen content of 13.40ppm showed to be sufficient for promoting HISC. The -800m$V_{Ag/AgCl}$ samples suffered from HISC, concluding that this will not be a safe potential

Sammendrag

Super Duplex Rustfritt Stål (SDSS) installert under havoverflaten har ved tidligere annledninger feilet under drift. Årsaken til dette har blitt konstatert å være Hydrogen Indusert Spenningssprekking (HISC). Effekten fra ulike beskyttelsespotensialer og hydrogeninnhold har blitt undersøkt for et Varm Isostatisk Presset (HIP) SDSS etter UNS S32550. Forladning har blitt gjort i en 2:1 Glycerol – H_3PO_4 elektrolytt ved 120°C, mens in-situ strekktesting er gjort i syntetisk sjøvann (3.5% NaCl) ved rom temperatur. Beskyttelsespotensialet har blitt variert mellom -1050m$V_{Ag/AgCl}$ til -800m$V_{Ag/AgCl}$.. Testing er blitt utført i en liten strekktestmaskin, hvor et lysmikroskopi er inkorporert i testapparaturen slik at det er blitt fulgt med på sprekkdannelser og andre mikrostrukturelle effekter. Ukjervede og kjervede prøver er blitt strekktestet. De ukjervede prøvene viste for stor duktilitet for testapparaturen og som følge av dette var det kun -1050m$V_{Ag/AgCl}$ prøvene som gikk til brudd ved 136±0% av flytespenningen. Det ble observert en sammenheng mellom overflatesprekkstørrelse og beskyttelsespotensial, hvor sprekkene ble større ved mer negative potensialer. De kjervede prøven gikk alle til brudd og følgende bruddstyrker ble ovbservert 136±0%, 137.3±1.9%, 144±0%, 148±0% and 140±0% av flytespenning for henholdsvis -1050m$V_{Ag/AgCl}$, -1000m$V_{Ag/AgCl}$, -950m$V_{Ag/AgCl}$, -900m$V_{Ag/AgCl}$ and -800m$V_{Ag/AgCl}$ prøvene. En kjervet prøve strekktestet i luft gikk til brudd ved 161% av flytespenningen. Den samme trenden for overflatesprekker ble sett på de kjervede prøvene, som på de ukjervede prøvene, hvor et mer negativt potensiale ga større overflatesprekker. Alle prøvene opplevde HISC, hvorav alle prøvene viste høy bruddstyrke. Et hydrogeninnhold på 13.40ppm viste seg å være nok for å få introdusert HISC. -800m$V_{Ag/AgCl}$ prøvene led av HISC, som følge av dette er det konkludert med at dette ikke er et trygt potensiale.

Preface

The present Master thesis is handed in as a part of the five year Master's degree program Materials Science and Engineering of the Norwegian University of Science and Technology. The work has been supervised by Professor Roy Johnsen, Post.Doc. Afrooz Barnoush and Ph.D. Jim Stian Olsen.

I would like to thank my supervisors for their guidance and help during this work. I would especially thank Post.Doc Afrooz Barnoush for the help I received in connection with setting up the pre-charging arrangement. I would also thank Nils-Inge J. Nilsen for helping with practical issues in the laboratory and Yingda Yu for his extensive help and knowledge when working in the SEM.

My co-students Adrian Haaland and Gaute Stenerud, who have worked with similar projects, have both been of good help and motivation during this period of time. And this is gratefully appreciated.

Declaration

I hereby declare that the present work is a product of my own work, which has been executed in accordance with the rules and regulations of the Norwegian University of Science and Technology.

Ola Myklatun Krosness
11. June 2014, Trondheim

Table of contents

Acronyms

Ag/AgCl	Silver/Silver chloride reference electrode
BCC	Body-Centered Cubic
CL	Constant Load
CP	Cathodic protection
DL	During Loading
DSS	22% Cr Duplex Stainless Steel
FCC	Face-Centered Cubic
FESEM	Field Emission Scanning Electron Microscope
HEDE	Hydrogen Enhanced De-cohesion
HELP	Hydrogen Embrittlement Local Plasticity
$Hg/HgSO_4$	Mercury/Mercury(II)sulfate
HIP	Hot Isostatically Pressed
HISC	Hydrogen Induced Stress Cracking
LVFESEM	Low Voltage Field Emission Scanning Electron Microscope
NaCl	Sodium chloride
NHE	Normal Hydrogen Electrode
RT	Room Temperature
SDSS	25% Cr Super Duplex Stainless Steel
SEM	Scanning Electron Microscope
SSRT	Slow Strain Rate Testing
UTS	Ultimate Tensile Strength
YS	Yield Strength

1 Introduction

Super Duplex Stainless Steel (SDSS) has been seen to be affected by Hydrogen Induced Stress Cracking (HISC) by recent failures in the oil and gas industry [1]. The common denominator for these failures is that the failed structures are all under cathodic protection (CP). SDSS on itself do not need any CP in sea water, because of its good corrosion resistance. But when connected to subsea structures needing CP, it is difficult to isolate the SDSS from the structure. Therefore SDSS used subsea is in most cases connected to a CP system. During CP hydrogen is evolved on the surface of the structure and hydrogen can diffuse into the SDSS and embrittle the material, leading to reduced strength and ductility. If high stresses are applied, the SDSS is more susceptible to failure. For HISC to occur, the combination of high stress, hydrogen and a susceptible material all needs to be present.

A new test setup is to be used in this work. The setup consists of small tensile test samples which are to be loaded in a small test jig with capacity of 10 000N. Testing is to be done in-situ, with a light microscope to scan the surface of the sample to detect cracks and other microstructural features. The setup was used in the foregoing project work and findings about operation are implemented in this Master thesis.

The purpose of the work is to investigate if there exists a hydrogen content limit for which HISC will not be an issue for SDSS. This is to be done by pre-charging samples at different potentials raging from -800m$V_{Ag/AgCl}$ to -1050m$V_{Ag/AgCl}$. This will represent the lowest potential were carbon steel will be protected and up to a typical operational protection potential. The different potentials will ensure different amount of hydrogen evolution and it is therefore believed to ensure different hydrogen content in the different samples. After testing samples are to be taken hydrogen measurements of and inspected in a SEM.

2 Theoretical background

As mentioned, in order for Hydrogen Induced Stress Cracking (HISC) to arise in a component, three factors must be present in the system. These three factors are a susceptible material, hydrogen and stress. This is illustrated by a Venn diagram in Figure 1.

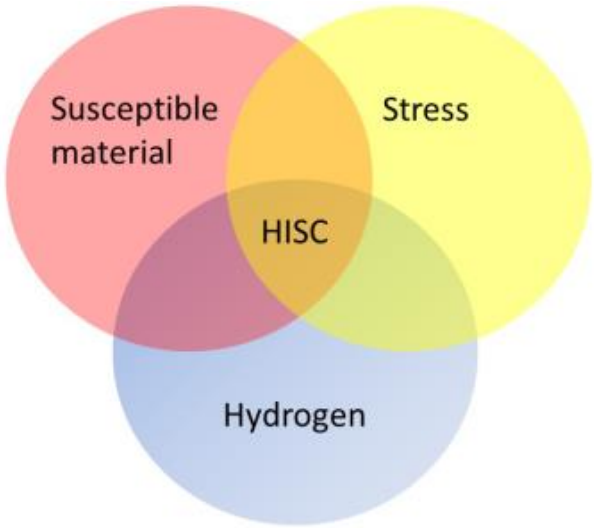

Figure 1 Venn diagram illustrating the three factors needed for HISC to arise. [2]

In general subsea components made of Super Duplex Stainless Steels and Duplex Stainless Steels (DSS) do not need any form of corrosion protection, due to the high corrosion resistance of these materials. But in most cases SDSS and DSS are used together with materials that do need corrosion protection [3]. A standard way of protection subsea components against corrosion is by using sacrificial anodes, this is referred to as cathodic protection (CP). This section will be addressing the three factors needed for HISC to arise, HISC in SDSS and previous work.

2.1 Hydrogen

The hydrogen can come from different sources, such as welding, general corrosion, unintended galvanic corrosion, but for the subsea application of SDSS the main source is the CP arrangement.

2.1.1 Hydrogen source

Sacrificial anodes, often zinc (Zn) and aluminium (Al) alloys, are connected to the subsea structure. This prevents the structure from corroding, since it lowers the corrosion potential of the structure down to a new potential called the couple potential (E_{couple}). At the E_{couple} the steel structure will now be in the immune region, this can be seen by the pourbaix diagram for steel, and hence protected from corrosion. This is illustrated in Figure 2, where an Evans diagram is seen.

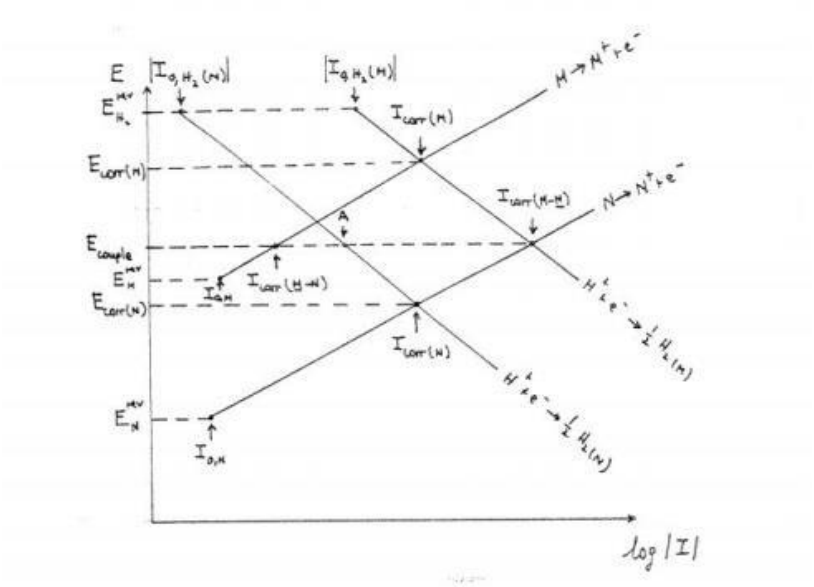

Figure 2 Evans diagram showing galvanic corrosion of metal N and the principal of cathodic protection of metal M. [4]

Initially before there is any connection between metal N and M, they will corrode at the $E_{corr(N)}$ and $E_{corr(M)}$, but when they are connected the new potential will be the E_{couple}. Now the corrosion rate of metal N is increased significantly, and the opposite is true for metal M. From this, one can also see that the more negative the E_{couple} potential becomes, more hydrogen will evolve at metal M [4]. For CP of structures with materials sensitive to HISC, as for SDSS, it is very important not to have an E_{couple} much lower than needed for protection of the structure, due to the hydrogen evolution mentioned. For carbon steel, the E_{couple} needed for protection is stated to be -800m$V_{Ag/AgCl}$ [5]. For design purposes the E_{couple} potential will lie in the range of -900 - -1050m$V_{Ag/AgCl}$. The hydrogen that evolves on the structure can either escape as hydrogen gas or it can be absorbed in the material as atomic hydrogen. The reactions associated with atomic hydrogen formation are according to equations 1 and 2 [6].

$$H_2O + e^- + \square \leftrightarrow H_{ads} + OH^- \quad (1)$$

$$H_{aq}^+ + e^- + \square \leftrightarrow H_{ads} \quad (2)$$

Where $\square$ represents a surface site, where hydrogen can be adsorbed onto. The adsorbed hydrogen can either diffuse into the material, equation 3, or leave the surface as hydrogen gas, equations 4 and 5.

$$H_{ads} \rightarrow H_{abs} \quad (3)$$

$$H^+ + H_{ads} + e^- \leftrightarrow H_2 + \square \quad (4)$$

$$H_2O + H_{ads} + e^- \leftrightarrow H_2 + OH^- + \square \quad (5)$$

2.1.2 Hydrogen diffusion

Hydrogen is the smallest and lightest atom that exist, because of this hydrogen has a very high mobility even at low temperatures [7]. Hydrogen will diffuse by interstitial sites in the lattice [8], but impurities, lattice faults, grain boundaries, non-metallic phases and the austenite phase itself will act as traps for the diffusing hydrogen [9, 10]. In the body-centred cubic (BCC) ferrite phase the lattice is open and not densely packed, this leads to a low solubility and high diffusivity. On the contrary, the face-centred cubic (FCC) austenite phase is a more closed and more densely packed lattice structure. Therefore a high solubility and low diffusivity is seen for this phase. These different properties are the main reason that hydrogen tends to diffuse through the ferrite phase and that the austenite phase acts as a trapping site for hydrogen in SDSS [10, 11].

The diffusion of hydrogen follows Fick's laws, and can therefore be calculated accordingly. The concentration difference is the driving force for diffusion in Fick's laws. Fick's 1st law is as follows [12]

$$J = -D\frac{\partial C}{\partial x} \quad (6)$$

Where J is the diffusion flux, $\partial C/\partial x$ is the concentration gradient and D is the diffusion coefficient given by

$$D = D_0 \exp\left(-\frac{E_a}{RT}\right) \quad (7)$$

Where D_0 is a material specific maximum diffusion coefficient, E_a is the activation energy, R the gas constant and T is the temperature. Equation 6 is good to use when the system is in a steady-state, but when this is not the case Fick's 2nd law is introduced.

$$\frac{\partial C}{\partial t} = -\frac{\partial J}{\partial x} \quad (8)$$

$$\frac{\partial C}{\partial t} = D\frac{\partial^2 C}{\partial x^2} \quad (9)$$

$$\frac{\partial C}{\partial t} = D\left(\frac{\partial^2 C}{\partial x^2} + \frac{\partial^2 C}{\partial y^2} + \frac{\partial^2 C}{\partial z^2}\right) \quad (10)$$

Equation 8 gives the conservation of mass and by combining equations 6 and 8 Fick's 2nd law for one dimension is obtained, here D is assumed to be independent of time and concentration. To find the concentration profile Fick's 2nd law needs to be solved, this can be hard for complex shapes. Equation 10 is Fick's 2nd law for three dimensions. The thick plate model is a solution to Fick's 2nd law. The model is a one dimensional plate with infinite length, a constant surface concentration C_i and an initial concentration throughout the specimen C_0. From this the concentration at a given time and distance C(x, t) is given by

$$\frac{C(x,t)-C_0}{C_i-C_0} = 1 - \mathrm{erf}\left(\frac{x}{2\sqrt{Dt}}\right) \quad (11)$$

Where erf is the error function given by

$$\mathrm{erf}(z) = \frac{2}{\sqrt{\pi}}\int_0^z (-\eta^2)d\eta \quad (12)$$

The model is illustrated in Figure 3

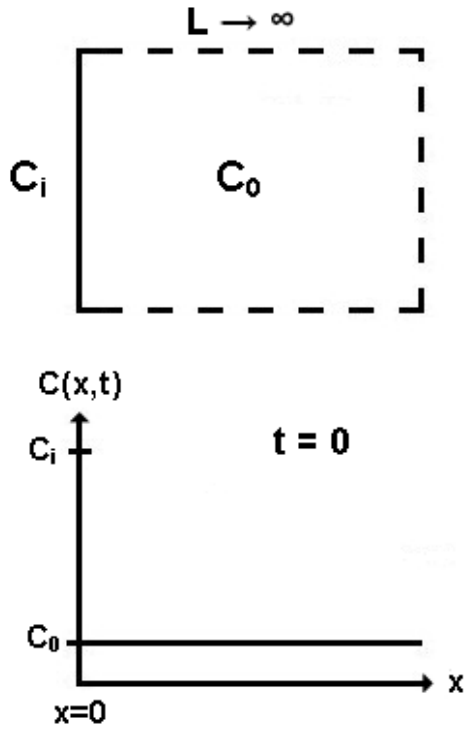

Figure 3 Illustration of the thick plate model. [13]

As t →∞ the internal concentration increases till it reaches C_i [13].

2.1.3 Hydrogen trapping

As mentioned, hydrogen can be trapped at different sites in the structure. This leads to a lower mobility of the hydrogen atom, and hence the diffusion speed is lowered [14]. There are different types of trap sites which hydrogen can be trapped. These trap sites is often categorized by the amount of energy the hydrogen atom needs in order to be released from the trap site. They can be divided into two main categories, reversible and irreversible traps. Reversible traps can release trapped hydrogen by tempering or high local strain [15]. Reported binding energies for reversible traps are often below 60 – 70 kJ/mol [14]. Irreversible traps cannot release hydrogen from the trap site in the applicable time and temperature range, this is due to the high energy gap associated with the irreversible trap sites.

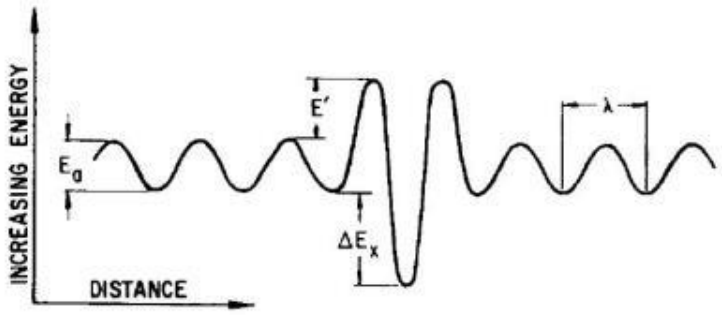

Figure 4 Schematic model of the energies related to a trap site. [16]

Figure 4 shows a trap site, E_a is the activation energy for the lattice sites, ΔE_x represents the energy difference for the trap site that is lower than for a normal lattice site, and the trap site is bounded by an energy barrier of height E' + E_a [16]. λ is the distance between the normal lattice sites [16].

$$D_{eff} = \frac{D_0 e^{\frac{-E_L}{RT}}}{1+\frac{N_T}{N_L} e^{\frac{-E_T}{RT}}} \quad (13) [6, 14]$$

D_{eff} is the effective diffusion coefficient taking reversible traps into account, N_L and N_T are the number of sites for hydrogen in the lattice and reversible trap sites, respectively. E_L and E_T are the binding energy in the lattice and at reversible traps (J/mol), respectively [6, 14]. The effect of reversible traps is described by equation 13 and one can note that the effect of reversible traps decrease with temperature and without any reversible traps equation 13 reduces to equation 7.

2.2 Stress

Stresses will arise in the structure from the operational loads, accidental loads, installation loads and misalignment. These loads contribute towards the susceptibility for HISC, only dependent by that the load has to be held for more than a couple of minutes and they have to be of a global manner [17]. Local stresses and strains can also affect the HISC susceptibility, Figure 5 shows the stress and strain field ahead of a crack tip. Hydrogen will accumulate on sites with increased hydrostatic pressure, i.e. a crack tip, and because of this embrittle the material in front of the crack tip and the crack will propagate. The effect on HISC in SDSS this phenomena has is debatable, according to Lauvstad et al [18] this is of influence towards HISC in SDSS.

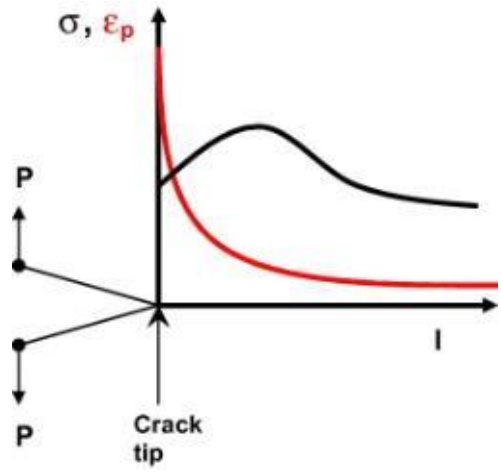

Figure 5 Schematic of hydrostatic pressure and strain field ahead of a crack tip. [15]

2.3 Super Duplex Stainless Steel

SDSS is a two phase material consisting of austenite and ferrite, these two phases have different properties and it is this that SDSS exploits to get its superior strength and corrosion properties. The corrosion resistance of the austenite phase and the strength of the ferrite phase. It should ideally be a 50/50 distribution of the phases, to get the best properties. The SDSS microstructure is often quantified with the average austenite spacing and the austenite spacing varies substantially with different production methods.

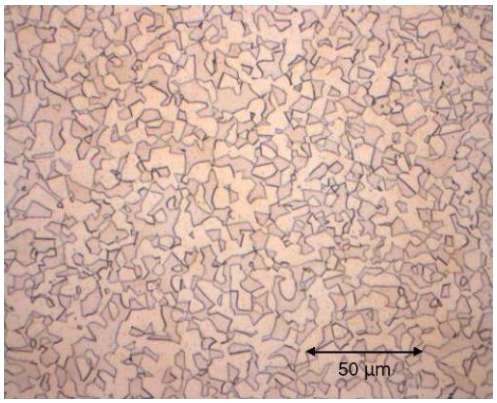

Figure 6 A Hot Isostatic Pressed Duplex Stainless Steel. Showing a small austenite spacing. [18]

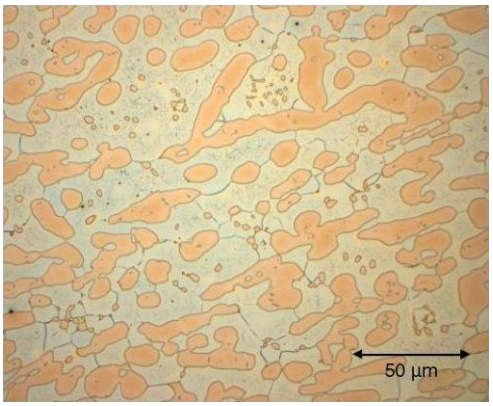

Figure 7 A forged Duplex Stainless Steel. Showing a large austenite spacing. [18]

Figure 6 and Figure 7 shows the different austenite spacing the same material can have due to different production methods, HIP and forged material respectively. In general the austenite spacing increases as you go from HIP to rolled plates to forgings [18].

2.4 HISC in Super Duplex Stainless Steel

Absorbed hydrogen embrittles the SDSS and causes SDSS components to fail in a brittle manner. The mechanism behind this embrittlement is not clearly understood. But there is developed different theories, the two most cited theories are the Hydrogen Embrittlement Local Plasticity (HELP) and the Hydrogen Enhanced De-cohesion (HEDE) models.

The HEDE model relates interstitial hydrogen to lowering the grain boundary de-cohesion or cleavage plane de-cohesion. This is due to the theory that the interstitial hydrogen dilates the atomic lattice and therefore lowers the fracture energy.
The HELP model is built up on that atomic hydrogen is enhancing the dislocation motion in specific crystallographic planes at the crack tip. Due to this cracking by micro voids coalescence along the softened grains occurs [14]. According to Olden recent research have found evidence supporting the HELP theory [19].

Fractures of metals are generally divided into two main fracture types, ductile and brittle. The process of fracture is divided into two components. First there is crack initiation and from this crack propagation follows. During ductile fracture, plastic deformation prior and during the crack propagation is seen. Rapid rate of crack propagation, with no global deformation and very little micro-deformation are features of brittle fracture [20]. Distinguishing the two fracture types is often done by using a scanning electron microscope (SEM) by looking at the fracture surfaces. Ductile fractures often show a "cup-and-cone" form of the fractured specimen. This fracture surface arises from the onset of necking, where a tri-axial stress state forms. This leads to formation of small voids, which start to grow together and perpendicular to the tensile stress axis until they come close to the surface and propagates along shear-planes at approximately 45° to the tensile stress axis and forms the "cup-and-cone" shape. Due to the coalescence of the voids during crack propagation the fracture surface will consist of elongated "dimples". This type of fracture surface is seen in Figure 8.

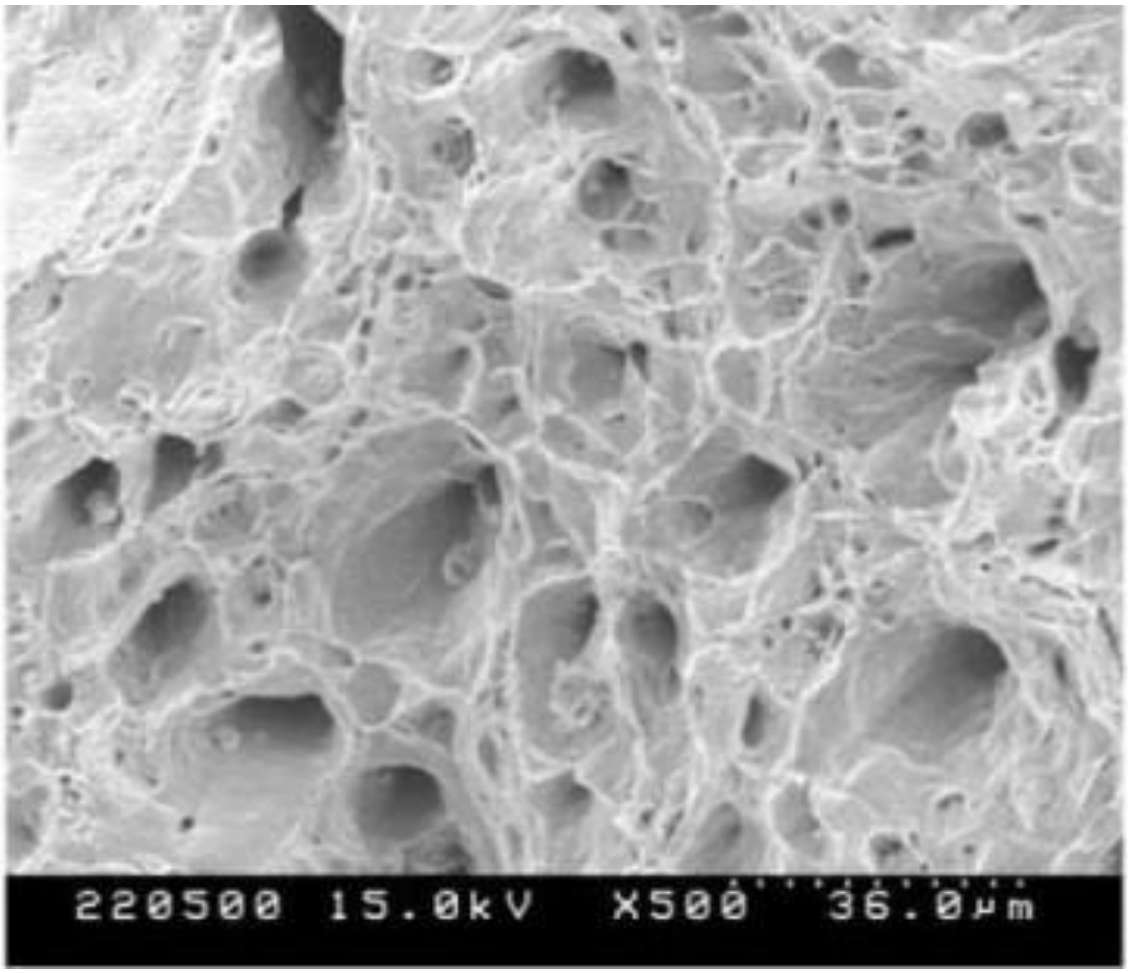

Figure 8 Ductile fracture surface from a Duplex Stainless Steel. The characteristic "dimples" are seen. [21]

There are generally two types of brittle fractures in metals, inter-granular and trans-granular. Trans-granular or cleavage fracture is characterized by flat facets with "river marking". Trans-granular cleavage occurs along crystallographic planes, therefore trans-granular. The "river marking" comes from the crack moving along parallel planes, and the direction of the "river pattern" is the same as the direction of the crack propagation. A fractograph of a trans-granular cleavage is seen in Figure 9. The preferred cleavage planes are those which are the less densely packed, and when the crack hits a grain boundary it will change direction. This is because the crack seeks the most favourable cleavage plane [22].

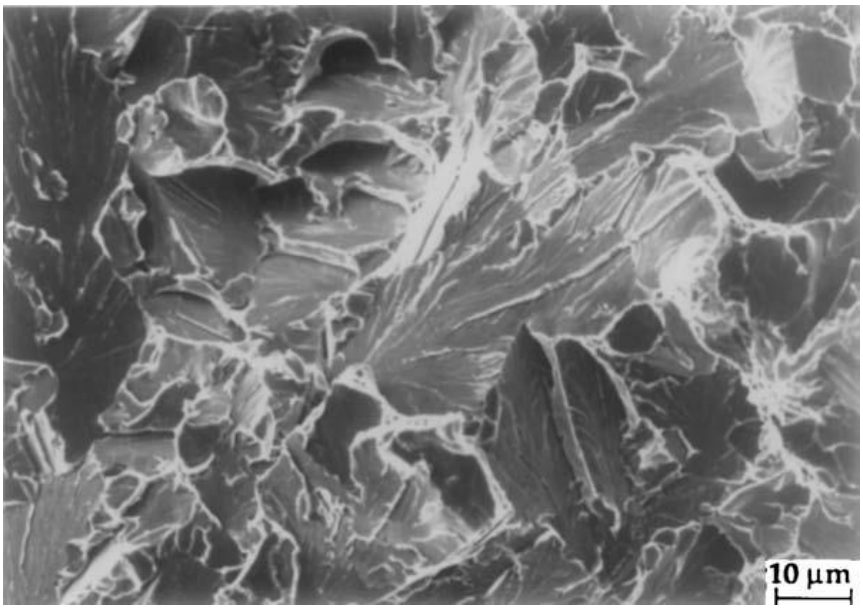

Figure 9 SEM fractograph of a trans-granular fracture in a low alloy steel. River patterns are seen, corresponding to the crack growth direction. [22]

Inter-granular fracture dos not commonly occur, but at some conditions where the grain boundaries are weakened it can occur. This can be brittle precipitates at the grain boundaries, grain boundary corrosion, environmental assisted cracking, etc. In a fractograph of an inter-granular fracture one can often see the grains along the fracture, this is seen in Figure 10.

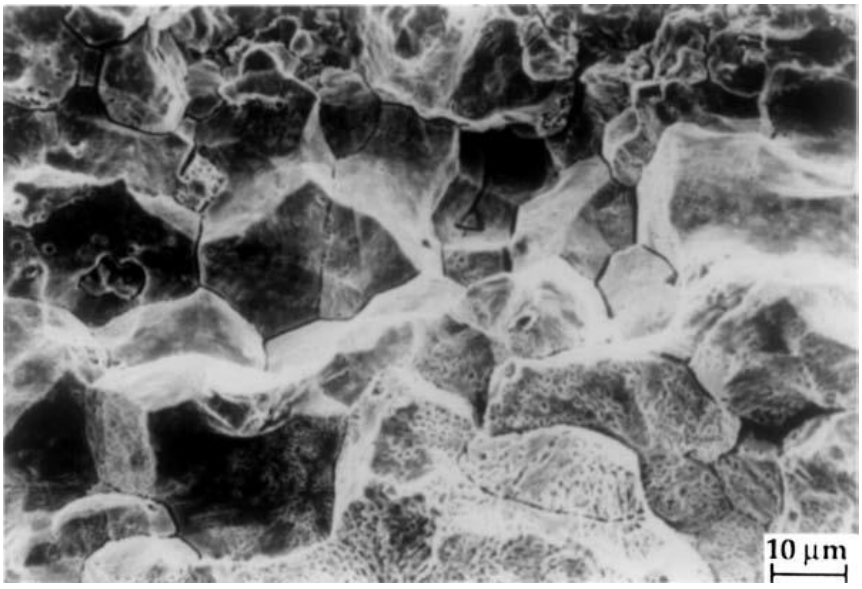

Figure 10 A fractograph of an inter-granular fracture in a steel. [22]

In SDSS trans-granular fracture and ductile fracture are the expected fracture modes. Due to the different properties of the austenite and ferrite phase, in a HISC fracture in SDSS ferrite tends to fail in a trans-granular manner while austenite fails in a ductile manner. This can be

seen in Figure 11 [15]. The low solubility of hydrogen in ferrite and its fast diffusion speed is the main reason for this to occur. This leads to the embrittlement of the ferrite. The opposite its true for the austenite phase, leading to the austenite phase often acts as a crack arrester. Figure 12 shows shallow cracks in SDSS, note that the cracks in general goes through the ferrite.

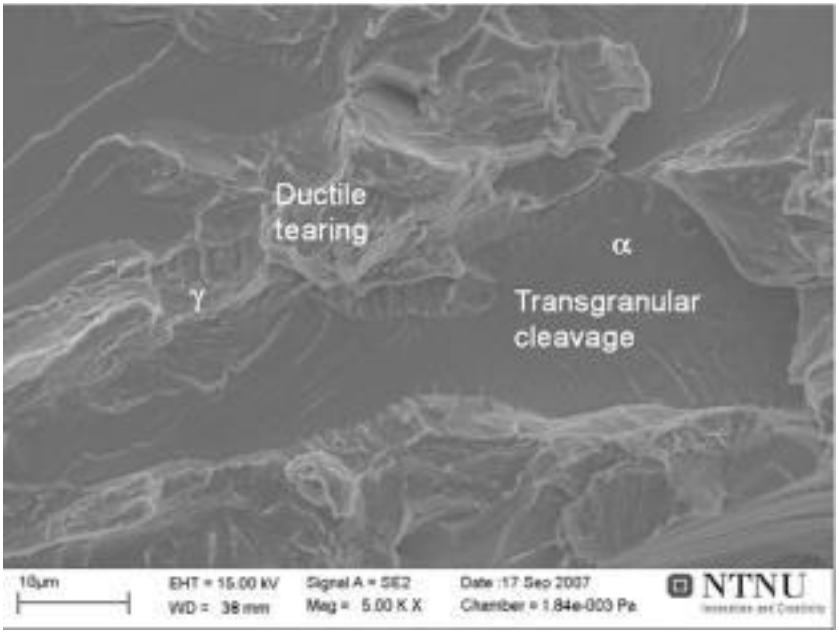

Figure 11 Fractograph of 25 % duplex stainless steel. [15]

Figure 12 Shallow cracks in a SDSS. [1]

Austenite will accordingly to Zakroczymski and Owczarek [10, 11] act as a trap site for hydrogen. Combining this with the diffusion of hydrogen through the ferrite phase gives an

explanation of why smaller austenite spacing will reduce the susceptibility for HISC [1, 15, 18]. Smaller austenite spacing will give a more tortuous path for hydrogen to diffuse through the ferrite, and hence slow down the ferrite diffusion.

2.5 Previous work

A literature review has been done to get a better understanding and updated view on relevant and interesting topics for the current scope of this Master thesis. Areas that have been giving extra attention are diffusion coefficients, effect of the protection potential, effect of hydrogen content, effect of grain size, effect of pre-charge, cold creep and stress threshold.

2.5.1 Diffusion coefficients

To understand the different diffusion coefficients for different steels and be able to relate them to the microstructure of the steels is of importance for understanding the diffusion in SDSS. Due to the two phase microstructure, the diffusion in SDSS is not straight forward. Olden et al. published a table with diffusion coefficients for different steels [14], this can be seen in Table 1. From this it is visible that the diffusion speed for hydrogen decreases from the most rapid in ferritic steel, to martensitic steel, to SDSS and is the slowest in austenitic steel. This relates to the unit cell for the different phases, as discussed earlier the diffusivity is higher in the BCC cell than the FCC cell and therefore the diffusion in ferritic steel is more rapid than in austenitic steel. The BCT unit cell of martensite is denser packed than BCC and therefore the diffusivity is between ferritic and austenitic. In the case of SDSS one could imagine that the diffusion coefficient should lie close to ferritic steel, this is clearly not true. This is explained by the austenite phase, which gives a more tortuous diffusion path and in addition the austenite/ferrite grain boundaries and the austenite phase itself acts as trap sites and slow the diffusion down [10, 11].

Table 1 Overview of reported diffusion coefficients in different steels. References refers to references in [14]. [14]

Steel	Alloy	Diffusion coefficient (m^2/s)	Charging conditions	Test temperature (°C)	Aust. cont. (%)	Ref.
Pure α-iron		7.2×10^{-9}	–	25	–	[12]
						[3,4,19]
		7.2×10^{-9}	–	22	–	"
		8.7×10^{-9}	–	50	–	"
		1.0×10^{-8}	–	80	–	"
Low alloy steel	X65	$1–2 \times 10^{-9}$	20 A/m^2 in 0.1N NaOH	25	–	[20]
		$4–5 \times 10^{-10}$	40 A/m^2 in 0.1 N NaOH	25	–	"
	M520	1.1×10^{-10}	−1050 mV SCE in 0.5 M NaCl	22	–	[31]
		1.9×10^{-11}	−900 mV "	22	–	"
		3.0×10^{-11}	−800 mV "	22	–	"
		5.5×10^{-11}	−1050 mV "	4	–	"
		2.5×10^{-11}	−900 mV "	4	–	"
		2.0×10^{-13}	−800 mV "	4	–	"
	HSLA 80	1.3×10^{-12}	10 mA in 0.1 M NaOH	25	–	[20]
	HSLA 100	4.5×10^{-13}	"	25		"
Ferritic stainless steel (heat-treated)	Fe–Cr	2.9×10^{-5}	–	70	–	[4]
	AL 29–4–2	6.1×10^{-7}	–	70	–	"
	SAF 2205	$4.9–5.5 \times 10^{-13}$	1 mA/cm^2 in 0.1 M NaOH	22	–	[3]
Martensitic stainless steel	PH 13–8	6.7×10^{-13}	1 mA/cm^2 in 0.1 M NaOH	–	–	[4]
	AISI 410	1.8×10^{-12}	"	–	–	"
Supermartensitic stainless steel	13Cr	2.5×10^{-13}	0.046 mA/cm^2 in 0.1 M NaOH	–	12	[4]
		3.0×10^{-13}	−1050 mV SCE in 0.5 M NaCl	22	–	[23]
		6.1×10^{-14}	"	4	–	"
	12CrNi Mo	1.6×10^{-9}	−1050 mV SCE in 3(%) NaCl	25	–	[22]
		6.9×10^{-10}	"	4	–	"
		8.2×10^{-10}	−900 mV SCE in 3(%) NaCl	4	–	"
	13CrNiMo	1.3×10^{-11}	H_2gas, 10^5Pa	70	<2	[24]
		1.2×10^{-12}	"	70	4.8	"
		1.0×10^{-12}	"	70	8.5	"
		7.2×10^{-13}	"	70	19.2	"
		6.0×10^{-13}	"	70	25	"
Duplex stainless steel	SAF 2205	$2.8–3.0 \times 10^{-15}$	1 mA/cm^2 in 0.1 M NaOH	22	49	[3,19]
Lattice diffusion		$1.0–1.5 \times 10^{-14}$	"	50	49	"
		$3.8–4.5 \times 10^{-14}$	"	80	49	"
With influence of traps		$1.1–1.4 \times 10^{-14}$	"	22	49	"
		$5.2–9.5 \times 10^{-15}$	"	50	49	"
Superduplex stainless steel						
Lattice diffusion	SAF2507	1.1×10^{-15}	1 mA/cm^2 in 0.1 M NaOH	22	49	[3,19]
		$4.5–5.2 \times 10^{-15}$	"	50	49	"
		$1.8–2.5 \times 10^{-14}$	"	80	49	"
With influence of traps						
		4.6×10^{-16}	"	22	49	"
	H25N5M	1.8×10^{-12}	10 mA/cm^2in 0.1 M NaOH	25	40	[2]
		1.0×10^{-13}	"	"	"	"
Austenitic stainless steel		$1.8–8.0 \times 10^{-16}$	–	–	–	[2]

From Table 2 the effect of increased grain size on the diffusivity is seen for the 2205 SDSS alloy. An increase in grain size leads to an increase in diffusivity. One can also note that the diffusivity of the austenite phase lies close to the diffusivity of pure austenitic steel, but the diffusivity of the ferrite phase is in the order of 10^2 smaller than in pure iron.

Table 2 Overview of reported diffusion coefficients in different SDSS.

Alloy	$D_{eff}[m^2/s]$	$D_\gamma[m^2/s]$	D_α $[m^2/s]$	Grain size austenite[μm]	Temp. [°C]	Ref.
H25N5M	1.8×10^{-12}	1.2×10^{-16}	1.5×10^{-11}	4 – 20 (cylindrical)	25	[10, 11]
2205	3.6×10^{-14}	-	-	7.59 (homogenous)	-	[23]
2205	6.4×10^{-14}			35	25	[24]

2.5.2 Effect of different polarization potentials

The polarization potential effects the amount of hydrogen produced at the cathode surface, hence the super duplex structure. The more negative potential, the more hydrogen will evolve at the surface, as mentioned earlier. Woollin and Gregori investigated the effect of different polarization potentials in respect to crack initiation and crack propagation [1]. Figure 13 shows how the strain is decreased with more increasingly negative potentials.

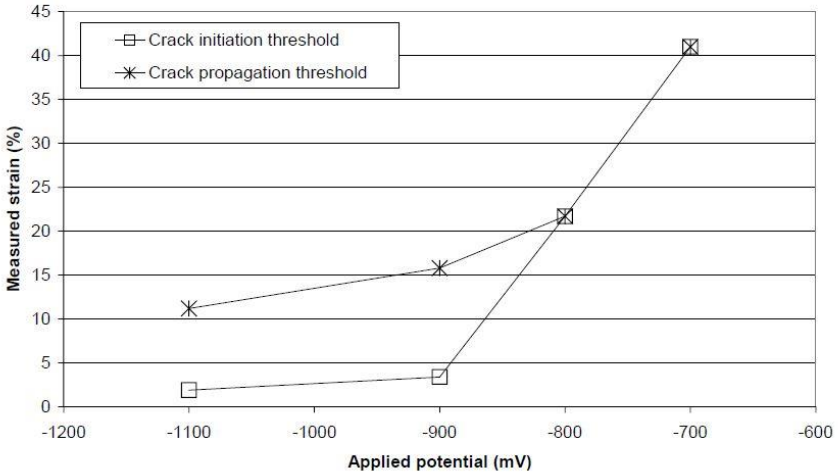

Figure 13 The effect of applied potential found by Woollin and Gregori. These results are from a bar with austenite spacing of 9 µm. [1]

According to An and Dobson the more negative potential applied, a higher amount of hydrogen entered into the SDSS and the embrittlement got more severe [25]. From Figure 14 and Figure 15 one can see the effect from different polarization potentials

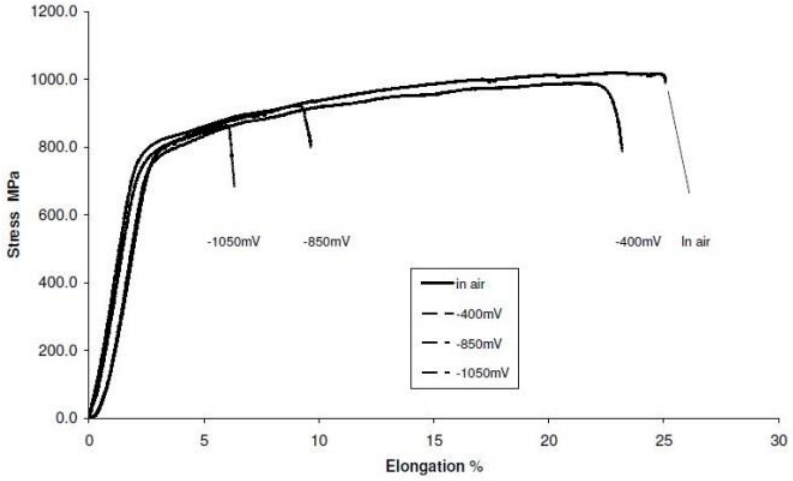

Figure 14 Stress strain curve obtained by SSRT testing of SDSS. The loss of ductility is significant when the potential gets more negavtive. [25]

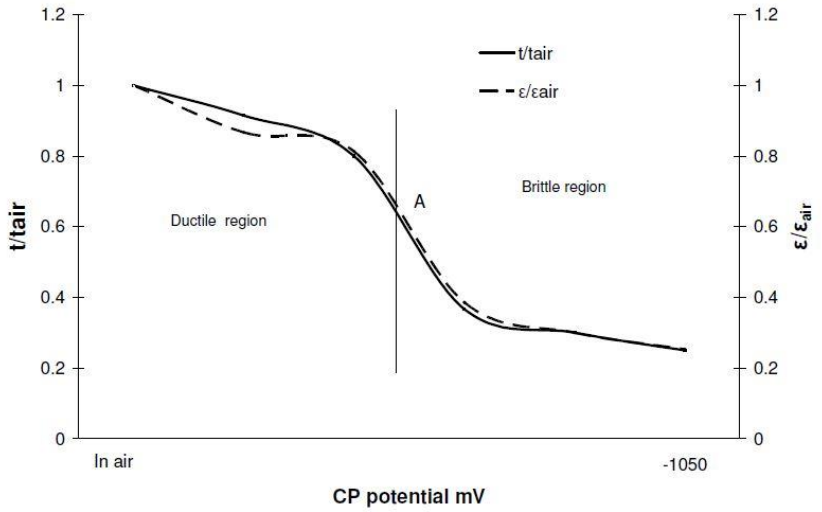

Figure 15 Curves showing the ratio of elongation and time to fracture compared to testing in air. Indicating a threshold potential exists, where HISC will not be an issue. [25]

Chang et al. performed SSRT and four point bending tests at different potentials. From the SSRT they found that the YS and UTS were not affected by cathodic polarization, even at polarization to -1150mV$_{Ag/AgCl.}$ The results only showed a reduction of ductility. The four point bending test was done with a load of 98% of YS and showed only small cracks when the potential was at -1050mV$_{Ag/AgCl}$ or lower. The cracks grew in size when the potential was shifted lower [26]. The specimens in this researched were pre-charged at 3°C for 30 days and hydrogen measurements were taken after testing. The specimens which did not show any cracks from the four point bend test, had as an highest average hydrogen concentration in the centre of the specimen 6ppm [26].

2.5.3 Effect of hydrogen content

Hydrogen is one of the three factors needed for HISC to occur. Zakroczymski et al. investigated the effect of increased hydrogen level on HISC in SDSS by SSRT. An increase in hydrogen content resulted in a higher grade of embrittlement, Zakroczymski et al. stated that the threshold for the total hydrogen level in order to get ductility loss is in the order of a few ppm wt. [27]. Figure 16 shows the reduction of ductility as a function of hydrogen content.

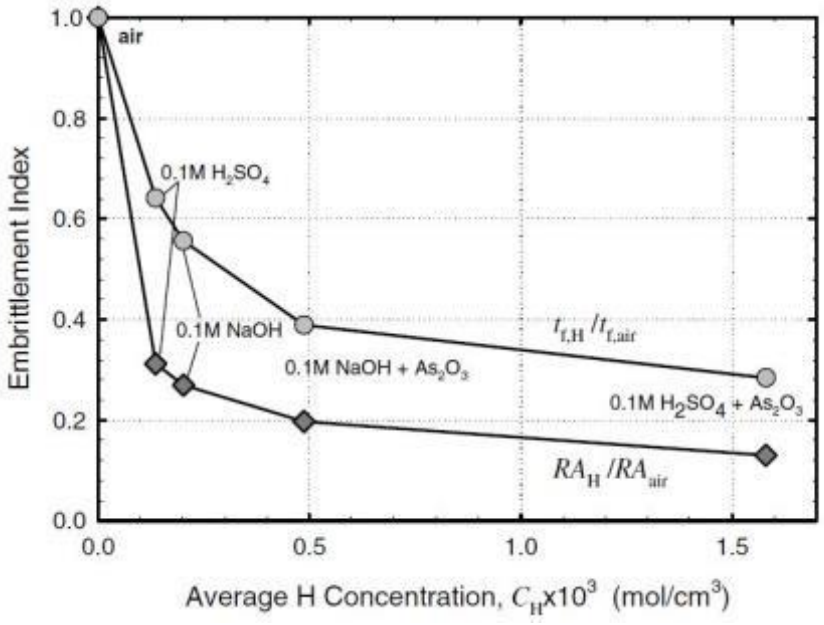

Figure 16 Showing the effect of hydrogen content on the ductility of SDSS. [27]

The hydrogen content measured by Zakroczymski et al. was the total hydrogen level, and therefore the surface content could have been much higher than a few ppm wt. Accordingly to this a few ppm wt. cannot be used as a critical value of hydrogen for HISC not to occur.

2.5.4 Effect of grain size

As discussed earlier a small grains size leads to a more tortuous diffusion path and therefore less hydrogen will diffuse in at a given time. Woollin and Gregori have quantified the effect of the austenite spacing and found that with a decrease in austenite spacing the threshold strain for HISC is increased [1]. This is seen clearly from Figure 17. This is also concluded by others [2, 18, 23, 28].

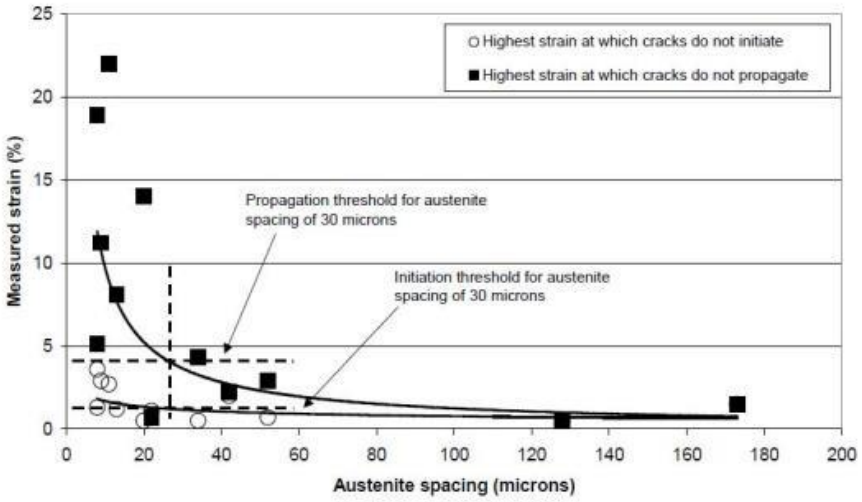

Figure 17 Strain threshold for HISC versus austenite spacing. [1]

There is also an understanding that the austenite phase acts as a crack arrester, which will have a positive effect on HISC threshold for smaller grain sizes. In addition Woollin and Gregori found that finer austenite grains lying between the "larger" austenite grains did not have any effect on arresting cracks [1].

2.5.5 Effect of pre-charging

Test samples are often pre-charged before testing. This has been done to ensure bulk hydrogen content in the samples. The effect of pre-charging the samples has been reported to be of varying importance. Kivisäkk and Holmquist reported no effect of pre-charging, though it should be noted that the samples were both pre-charged and tested at 80°C [29]. Griffiths and Turnbull pre-charged the samples at 80°C and the tested them at 20°C found also that pre-charging did not have any significant effect. This was suggested to be because of the local hydrogen uptake at oxide film rupture sites and at crack initiation sites from the surface of the samples, to be of more importance than the bulk hydrogen [30]. On the contrary Lauvastad et al. reported a significant effect of pre-charging. In this study the pre-charging was done at room temperature (RT) and the testing mainly at 4°C. It was suggested that the effect of pre-charging would strongly be affected by the following testing conditions for the samples. Hsu et al. investigated the effect of pre-charging time, the effect is quantified with the depth of the embrittled layer in round tensile test specimen tested with SSRT. They found a correlation between the embrittlement and charging time corresponding to the embrittled layer depth being proportional to the square of the time [31].

2.5.6 Cold creep

Cold creep is similar to ordinary creep, the difference lies in the temperature which it occurs. Ordinary creep is expected only to be of importance at elevated temperatures, but for SDSS it is seen that cold creep is of significance at lower temperatures [32]. Woollin and Gregori showed that cold creep of a super duplex bar, with austenite spacing of 20μm was in order of 2.7 % strain when the bar was loaded till 98 % of the YS [1].

2.5.7 Stress threshold

Andersen found an average stress threshold for fracture to be 123 % of YS with a standard deviation of 5.6 % on the same material investigated in this work, the sample also showed secondary cracks [2]. The tests were done with round bar specimens in Cortest Proof rings in a two stage manner, first at a constant load for 1 day and then an increase of 4 % of YS with 1 day intervals. Kivisäkk reported for a UNS S32750 SDSS, with austenite spacing between 9.4 and 16.1 μm, in a constant load test using dead weight, that no cracks were observed at 130 % of YS [33]. Ronneteg et al. performed constant load dead weight tests on varying production forms and found for austenite spacing in order of 15μm, the specimens withstood 130% of YS without any cracks forming. For this study, the samples were pre-charged with constant current and no reference till potentials has been mentioned [34].

3 Material and experimental method

The main purpose of the present work was to investigate if there is a hydrogen concentration limit, where HISC will not occur. This is done by pre-charging at different protection potentials.

3.1 Material

The SDSS investigated in this work was of grade UNS S32550 and produced by Hot Isostatic Pressing. The material was supplied by Aker Solutions ASA. Table 3 and Table 4 show the chemical composition and the mechanical properties of the material, respectively. These properties was taken from Andersen's master thesis [2], which was done with the same material.

Table 3 The chemical compostion of the material used. Values are given in wt%.

Grade	C	Si	Mn	P	S	Cr	Ni	Mo	Cu	W	N
UNS S23550	0.016	0.44	1.32	0.012	0.003	25.9	6.4	3.21	1.78	0.02	0.25

Table 4 Mechanical properties and microstructural features of the material used.

Grade	Yield strength [MPa]	Tensile strength [MPa]	Elongation [%]	Ferrite [%]	Austenite spacing [µm]
UNS S23550	653.3	888.5	39.8	46.0	12.9

The testing was done in the same test rig as used in the foregoing project work. Two sample geometries were tested, one without notch and one with. The sample geometries are seen in Figure 18 and Figure 19.

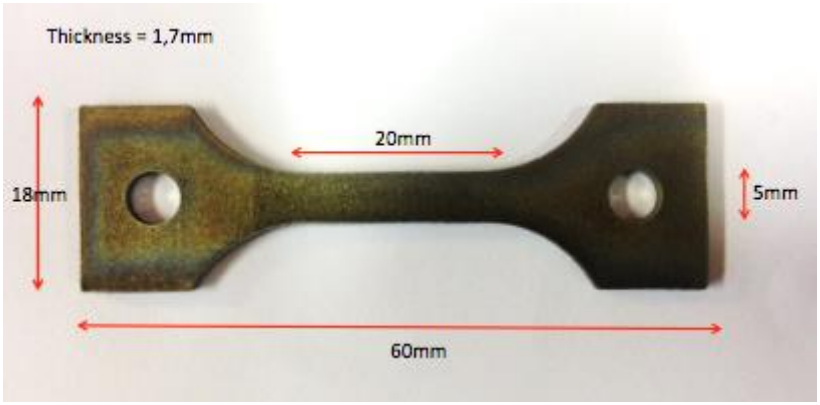

Figure 18 An overview of the non-notched sample.

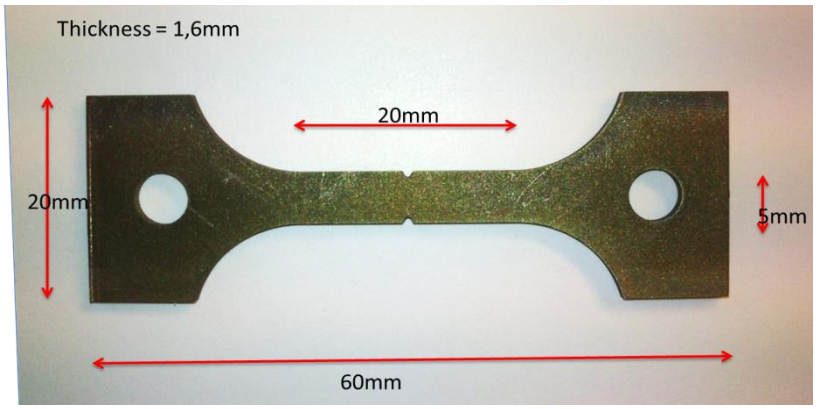

Figure 19 An overview of the notched sample. Note that the notch is of depth 0.6mm, 60° sidewall angle and a tip radius of 0.3mm.

3.2 Test matrix

Both the non-notched and notched samples were all pre-charged before in-situ tensile testing. The testing was done according to Table 5 and Table 6. The pre-charging was done in a 2:1 Glycerol – H_3PO_4 solution, this was done because it enables a higher operational temperature, e.g. more hydrogen in a shorter time period. The tensile testing was done in a 3.5 % NaCl solution, this was to be consistent with the foregoing project work. The testing were made up of three stages; pre-charging, constant stress and increasing stress. The constant stress stage was of 2 hours and 45 minutes, this was because the test should be possible to run within one day. The initial constant stress was decided as 95 % of the fracture load found for samples pre-charged at -1050m$V_{Ag/AgCl}$ in the foregoing project work.

Table 5 Test parameters for the tensile testing.

	-1050mV$_{Ag/AgCl}$	**-1000mV$_{Ag/AgCl}$**	**-950mV$_{Ag/AgCl}$**	**-900mV$_{Ag/AgCl}$**	**-800mV$_{Ag/AgCl}$**	**In air**
Number of samples	2 non-notched / 3 notched	3 non-notched / 3 notched	3 non-notched / 3 notched	3 non-notched / 3 notched	3 notched	1 notched
Pre-charge solution	2:1 Glycerol – H_3PO_4	2:1 Glycerol – H_3PO_4	2:1 Glycerol – H_3PO_4	2:1 Glycerol – H_3PO_4	2:1 Glycerol – H_3PO_4	-
Tensile test solution	3.5 % NaCl	3.5 % NaCl	3.5 % NaCl	3.5 % NaCl	3.5 % NaCl	-
Stage 2 stress	124 % of YS	124 % of YS	124 % of YS	124 % of YS	124 % of YS	138 % of YS
Stage 3 stress	Increment before + 4 % of YS	Increment before + 4 % of YS	Increment before + 4 % of YS	Increment before + 4 % of YS	Increment before + 4 % of YS	Increment before + 4 % of YS

Table 6 Test parameters for the tensile testing.

	Pre-charging	**Stage 2 Constant stress**	**Stage 3 Increasing stress**
All samples	5 days, T = 120°C	2h 45min, T = RT	Each hour until fracture, T = RT

3.3 Sample preparation

The samples were prepared according to the procedure used in the foregoing project work. This consisted of the following steps:

1. Mechanically grinded at: 800 grit – 1200 grit
2. Mechanically polished at: 3µm - 1µm
3. Electro polished in a 5 % H_2SO_4 / methanol electrolyte for 30 seconds at 25 V.

Since the samples were only to be looked at from one side, the last step was only done on one side of the samples, and in the parallel region. The rest of the procedure was done on the entire sample, this to avoid contamination from residues on the sample while pre-charging.

3.4 Pre-charging

The pre-charging was done in a 2:1 glycerol – H_3PO_4 electrolyte. The setup consisted of a boiling flask sunken in an oil bath, an $Hg/HgSO_4$ reference electrode and platinum wires as counter electrodes. Table 7 summarizes the potentials for the different reference electrodes used.

Table 7 Overview of the different reference electrodes and the corresponding potentials. [35]

Reference electrode	E vs NHE [V]	E [mV] corresponding to -1050mV$_{Ag/AgCl}$
Ag/AgCl (saturated KCL)	0.198	-1050
$Hg/HgSO_4$	0.654	-1506

The setup can be seen in Figure 20. The pre-charging was done at 120°C, for 5 days and done with 1, 3 or 4 samples in the flask. Generally the pre-charging setups consisted of 3 samples. A Gamry Interface 1000™ potentiostat was used to control the potential, this was coupled to a computer and the current/voltage curves were obtained.

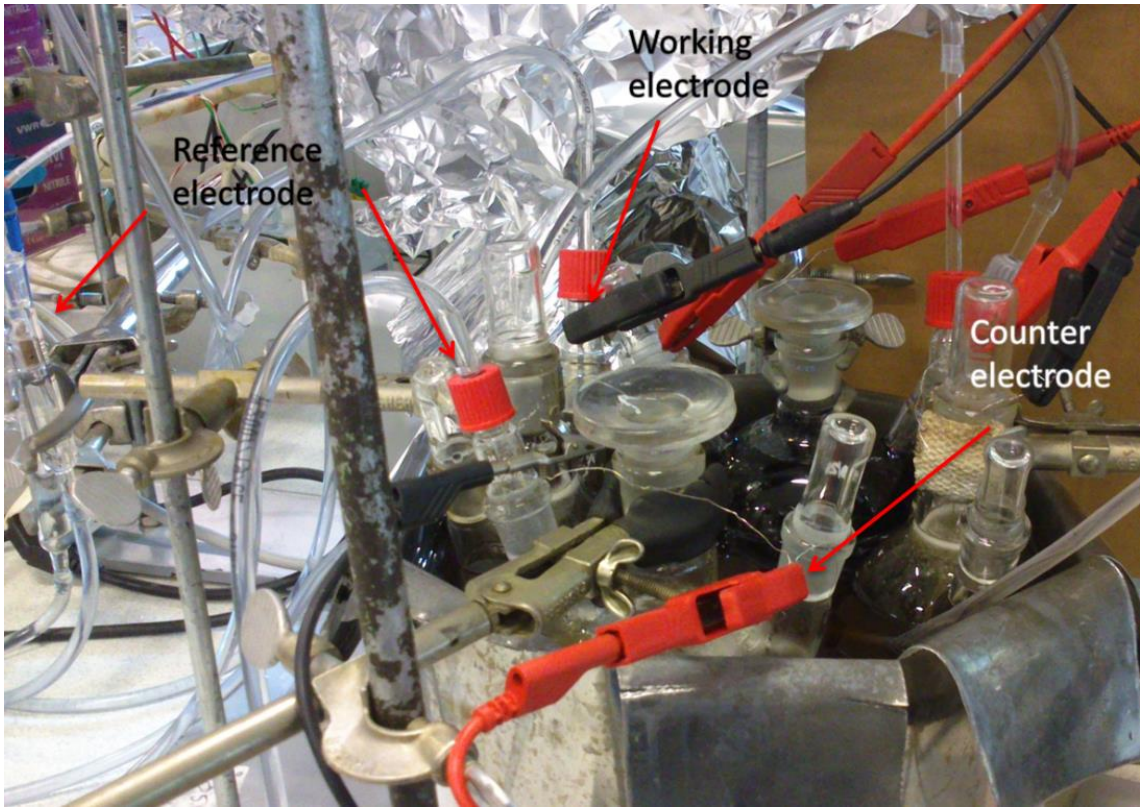

Figure 20 The pre-charge setup used. Note that the reference electrode tag refers to both the reference electrode and the reference electrode inlet for the flask.

After the pre-charging the samples were washed by an ultrasonic cleaner in alcohol and then put straight in a freezer. The samples were kept in the freezer until they were to be tensile tested.

3.5 Tensile testing

The tensile testing was done according to the test matrix described. The samples were put in a plastic chamber and then loaded in the tensile test machine, except the sample tested in air. The electrolyte used during tensile testing was 3.5 % NaCl, the counter electrode was a platinum wire and an Ag/AgCl reference electrode was used to control the potential. The setup is seen in Figure 21 and Figure 22.

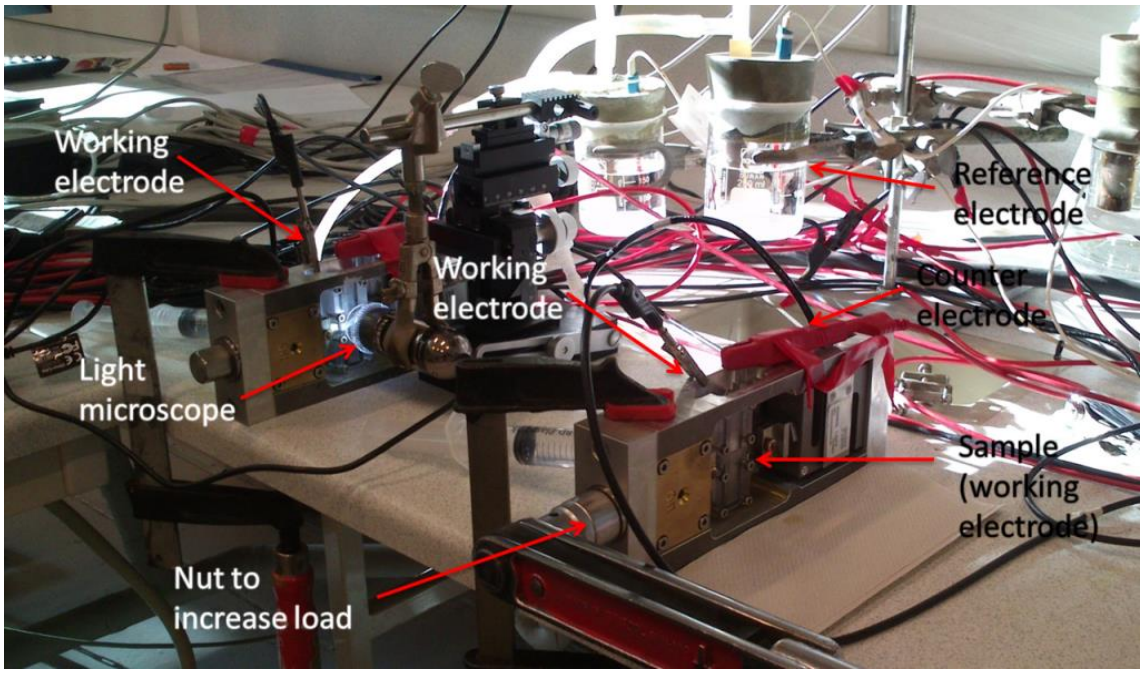

Figure 21 An overview of the tensile test setup.

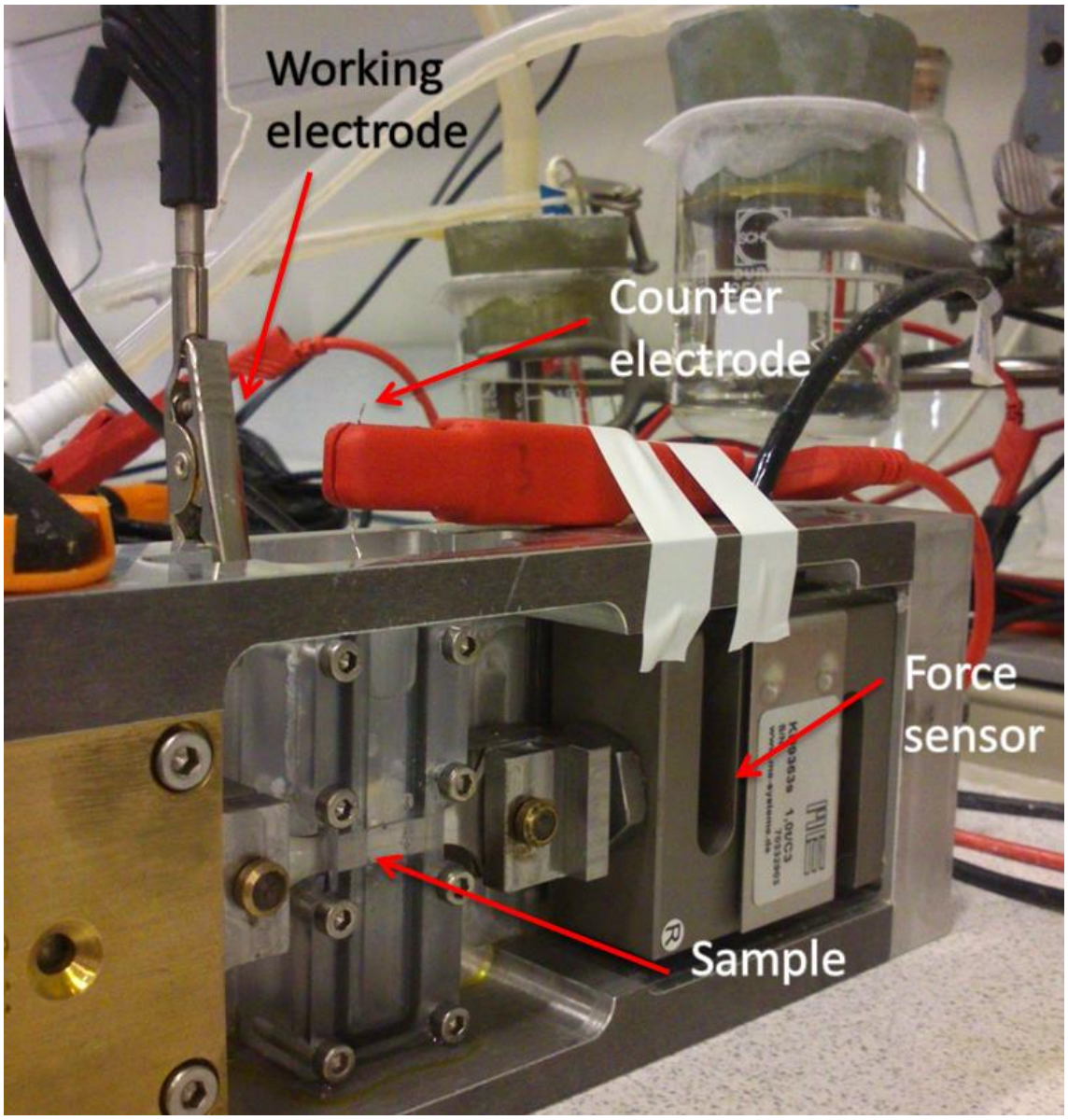

Figure 22 A closer look at the tensile test setup, here without the light microscope. There are a inlet and outlet on the backside og the chamber, enabling the tube from the reference electrode to connect.

The tensile test machine utilise a force sensor from ME Systeme GmbH designated KD9363S with a load range of 1 ton. The load curve is obtained by the program GSV-Control supplied by the producer of the force sensor. The optical microscope used is from Dino-Lite TM, and are operated by a xyz-stage from World Precision Instruments (WPI). The load is adjusted by using a wrench to screw the nut seen in Figure 21. The tests were run using the same potentiostat as in the pre-charging setup, and a current/potential graph was obtained from the tests.

3.6 Crack initiation test

To investigate the usability of the current/potential curves from the tensile testing, in reference to crack initiation, one non-notched sample pre-charged at -1050mV$_{Ag/AgCl}$ was tensile tested according to the same procedure as described in chapter 3.6, except the test was to be stopped when a crack was indicated by the current/potential graph and to aid this the light microscope was used.

3.7 Fracture surface examination

All the samples were examined in a Scanning Electron Microscope (SEM). A FESEM Zeiss Ultra 55 Limited Edition and a LVFESEM Zeiss Supra 55 VP were used for the examination. The fracture surface and the specimen surface were examined. The samples were cleaned ultrasonically in ethanol, before they were inserted into the SEM. The SEM was run at 20 keV and the secondary electron detector was used.

3.8 Hydrogen measurements

Hydrogen measurements were to be taken from each parallel of the notched samples, one sample from each parallel was selected. The hydrogen measurements were taken by SINTEF.

4 Results

4.1 Pre-charging

During the pre-charging process some issues did arise, some of the setups lost contact with the reference electrode during the 5 days, resulting in an uncontrolled current. The -900mV$_{Ag/AgCl}$ and -950mV$_{Ag/AgCl}$ notched samples where without potential for approximately the 6 last hours, due to the computer updating. The electrolyte needed to be changed for most of the setups at intervals from 1 till 2 days, because the electrolyte decomposed and blackened. The amount of decomposition varied with potential, more negative potential gave a higher decomposition rate. The -800mV$_{Ag/AgCl}$ notched samples had strange potential/current features, without any obvious explanation. This is seen in Figure 24 (e). Table 8 summarizes issues that arose during pre-charging. As one can see from Figure 23 and Figure 24 the pre-charging was rather unstable, note that the biggest peaks have arisen when the electrolyte has been changed.

Table 8 Overview of issues that arose during the pre-charging

	-1050mV$_{Ag/AgCl}$	**-1000mV$_{Ag/AgCl}$**	**-950mV$_{Ag/AgCl}$**	**-900mV$_{Ag/AgCl}$**	**-800mV$_{Ag/AgCl}$**
Non-notched	Unprotected for a couple of hours.	Generally unstable.	Generally good.	Lost reference electrode for 1 hour -> pos. current.	-
Notched	Very unstable. Lost reference electrode for some hours.	Generally good, but a bit unstable.	Good, 4 samples in the flask.	Unstable, 4 samples in the flask	Good, but some strange potential increases.

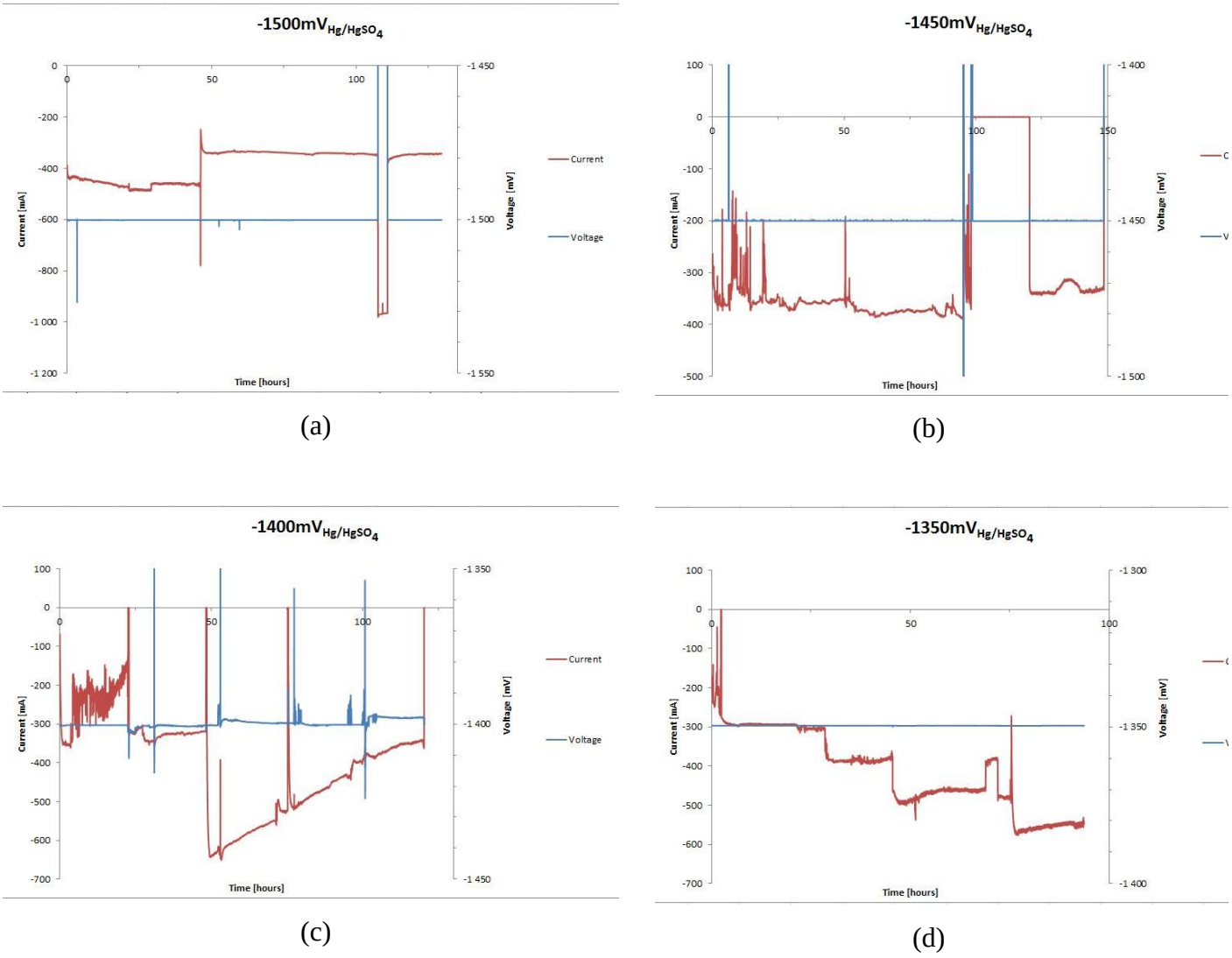

Figure 23 Current/potential graphs from the pre-charging of the non-notched samples. (a) -1050mV$_{Ag/AgCl}$, (b) -1000mV$_{Ag/AgCl}$, (c) -950mV$_{Ag/AgCl}$, (d) -900mV$_{Ag/AgCl}$.

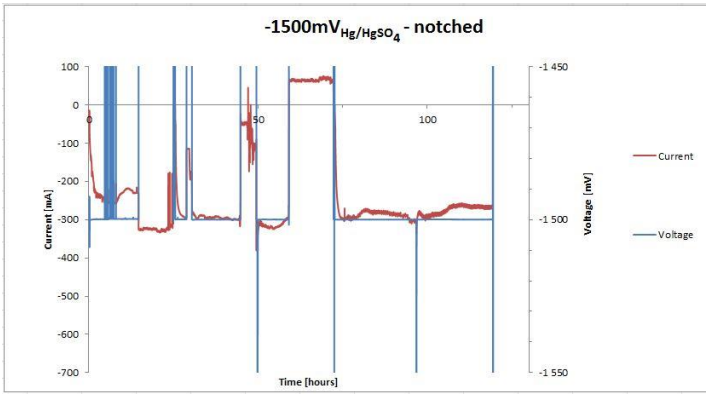

(a)

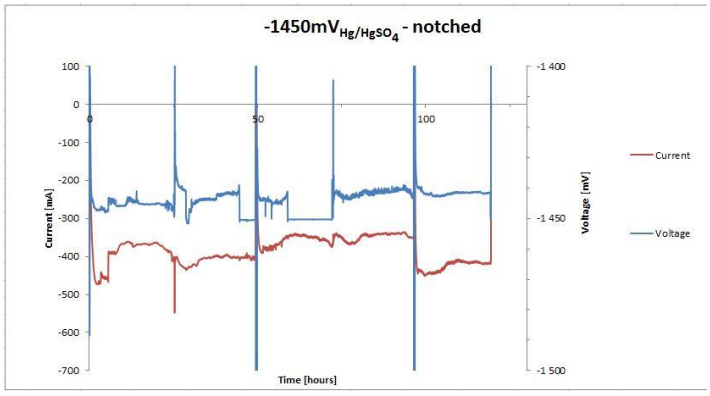

(b)

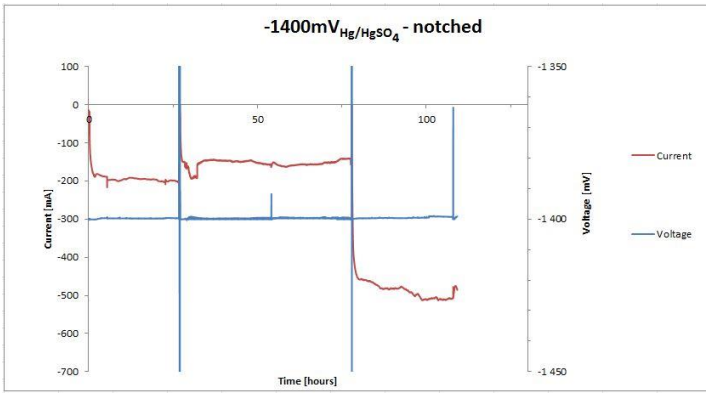

(c)

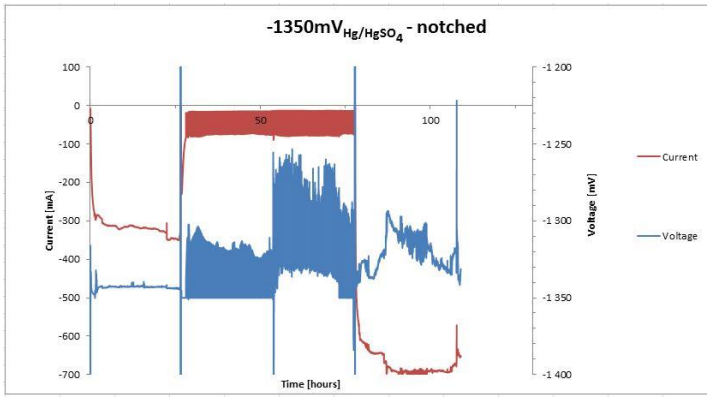

(d)

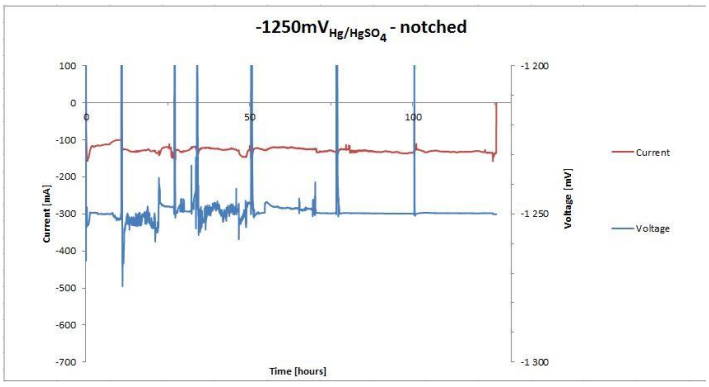

(e)

Figure 24 Current/potential graphs from the pre-charging of the notched samples. (a) -1050mV$_{Ag/AgCl}$, (b) -1000mV$_{Ag/AgCl}$, (c) -950mV$_{Ag/AgCl}$, (d) -900mV$_{Ag/AgCl}$ and (e) -800mV$_{Ag/AgCl}$

4.2 In-situ tensile testing

The in-situ tensile testing was done accordingly to the test matrix. The samples experienced cold creep during the testing, in order of approximately 2-4 % of YS. The amount of creep was lower for the notched samples. The creep was continuously adjusted for. The sealing of the chambers was successful of varying character, and electrolyte was filled when needed. The effect of this is clearly seen in the current/potential graphs, were a distinct drop in current is seen. When a critical crack was seen, the samples where either pulled to fracture or the crack was let to propagate at its own speed.

4.2.1 Non-notched samples

It was only the -1050mV$_{Ag/AgCl}$ samples that fractured, the other samples were to ductile for the tensile test machine. Because of this, samples with a notch were made. The -1050mV$_{Ag/AgCl}$ samples fractured at the 136% load stage, but both samples had a maximum applied load of 138±0% of YS. Both samples fractured while held at the 136% load stage.

Table 9 Overview of the load step that was reached during in-situ tensile testing of the non-notched samples. Note that the two -1050mV$_{Ag/AgCl}$ samples fractured. The values are from sample 1 to sample 3, from left to right.

	-1050mV$_{Ag/AgCl}$		**-1000mV$_{Ag/AgCl}$**			**-950mV$_{Ag/AgCl}$**			**-900mV$_{Ag/AgCl}$**		
Load step reached	136% (fract-ured)	136% (frac-tured)	136%	136%	136%	140%	140%	136%	136%	136%	140%

The reason for the different load steps reached is because of inconsistent adjustment of the creep. So any conclusions from the different load steps reached are not possible to draw. Figure 25 shows a typical stress-time graph from the in-situ tensile tests.

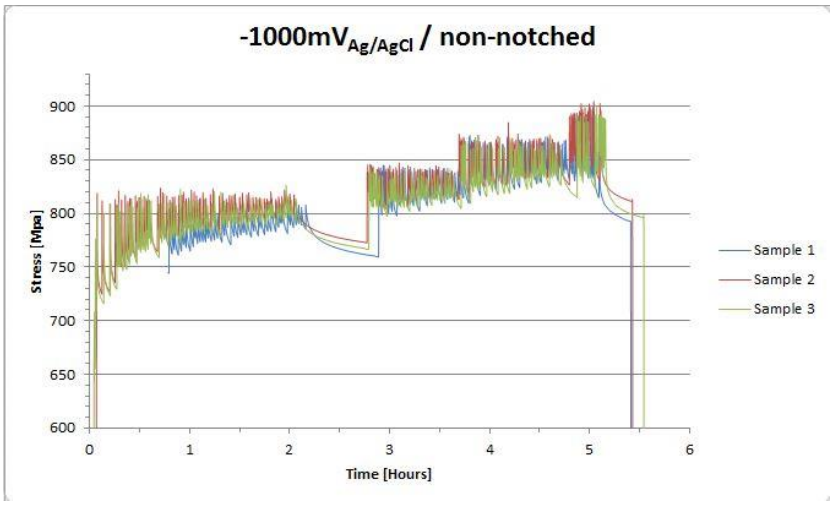

Figure 25 Stress-time graph showing the stress history from the in-situ tensile test of the -1000mV$_{Ag/AgCl}$ samples. The graph shows a typical result for the in-situ tensile tests, therefore only one graph is included.

During the tensile test light microscopy photos were taken. Generally the first small cracks were hard to discover, but when they grew in size they were taken photos of. One could see hydrogen forming and escaping from the cracks. Figure 26 shows cracks in the sample 2 - 1000mV$_{Ag/AgCl}$ at the 132% and 136% load step, respectively (a) and (b).

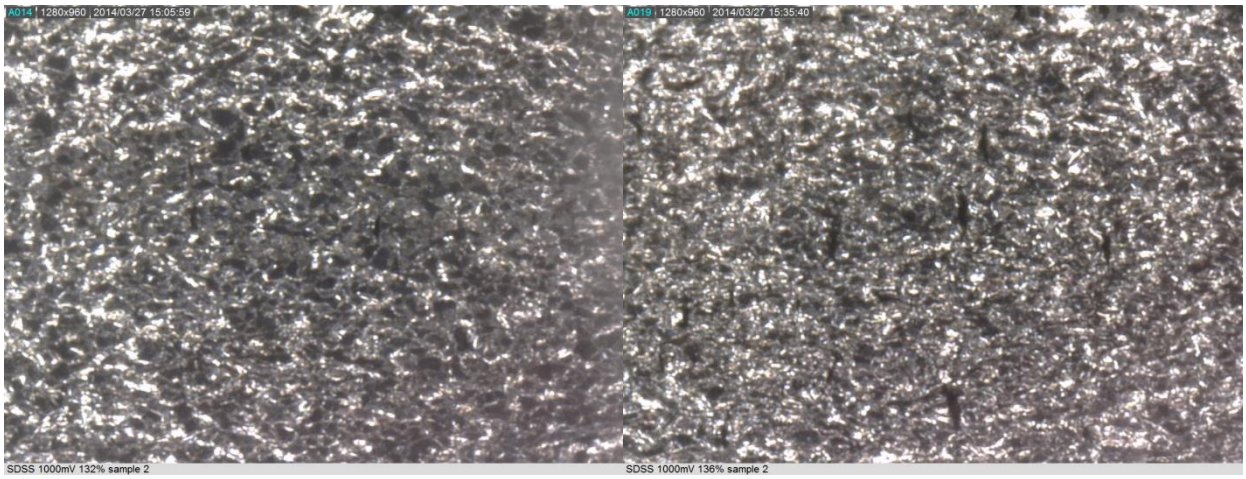

(a) (b)

Figure 26 Light microscopy photos from the in-situ tensile test of the non-notched -1000mV$_{Ag/AgCl}$. (a) shows the sample at 132% of YS and (b) shows the sample at 136%. Note the increase in crack size.

Similar photos were taken for all the samples, the trend saw smaller cracks at more positive potentials. It was noted on which load steps it was possible to see cracks, the results are seen in Table 10. Note that the optical microscope in this setup did not have good enough resolution to detect cracks smaller than around 30μm.

Table 10 Summary of the load steps cracks was first seen in the non-notched samples. Note that the optical microscope in this setup did not have good enough resolution to detect cracks smaller than around 30µm.

	-1050mV$_{Ag/AgCl}$	**-1000mV$_{Ag/AgCl}$**	**-950mV$_{Ag/AgCl}$**	**-900mV$_{Ag/AgCl}$**
Non-notched	Hydrogen evolution seen at 132% suggesting cracks. Cracks seen at 136%	Cracks seen at 132%	Cracks seen at 136%	No cracks seen. (Cracks found in SEM)

Current potential curves were obtained for all samples, in general there are a lot of disturbance to the curves. The current/potential curve for the same sample as in Figure 26 is seen in Figure 27.

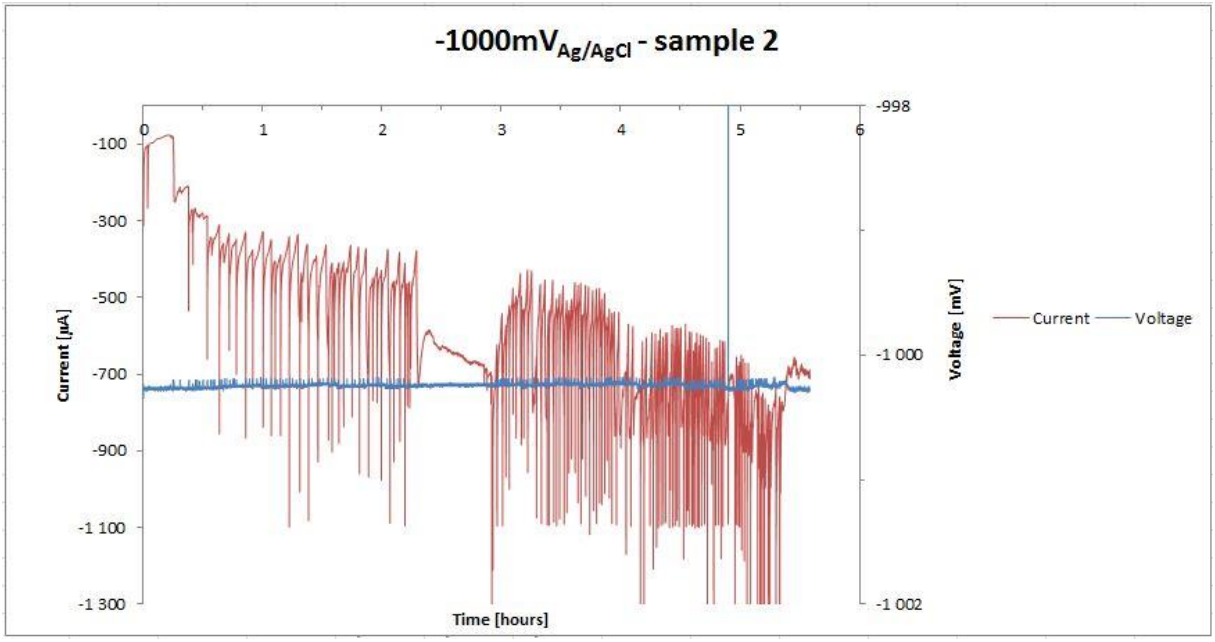

Figure 27 The current/potential graph for the -1000mV$_{Ag/AgCl}$ sample 2.

4.2.2 Notched samples

The notched samples were tested according to the test matrix. All the samples fractured.

Table 11 Overview of the fracture loads from the in-situ tensile test of the non-notched samples. Note that the -800mV$_{Ag/AgCl}$ samples fractured at a lower stress than both -950mV$_{Ag/AgCl}$ and -900mV$_{Ag/AgCl}$. CL stands for constant load and DL stands for during loading. The values are from left to right, respectively sample 1 to sample 3.

	-1050mV$_{Ag/AgCl}$			-1000mV$_{Ag/AgCl}$			-950mV$_{Ag/AgCl}$			-900mV$_{Ag/AgCl}$			-800mV$_{Ag/AgCl}$			Air
Fracture stress [% YS]	136 % CL	136 % CL	136 % CL	136 % CL	136 % CL	140 % DL	144 % CL	144 % CL	144 % CL	148 % CL	148 % CL	148 % CL	140 % CL	140 % CL	140 % CL	-
Avg. fracture stress [% YS]	136%±0%			137.3%±1.9%			144%±0%			148%±0%			140%±0%			-
Highest stress [% YS]	137 %	137 %	137 %	137 %	137 %	141 %	146 %	145 %	143 %	149 %	148 %	149 %	140 %	140 %	141 %	161 %
Avg. highest stress [% YS]	137%±0%			138.3%±1.9%			144.7%±1.3			148.7%±0.5			140.3%±0.5			161 %

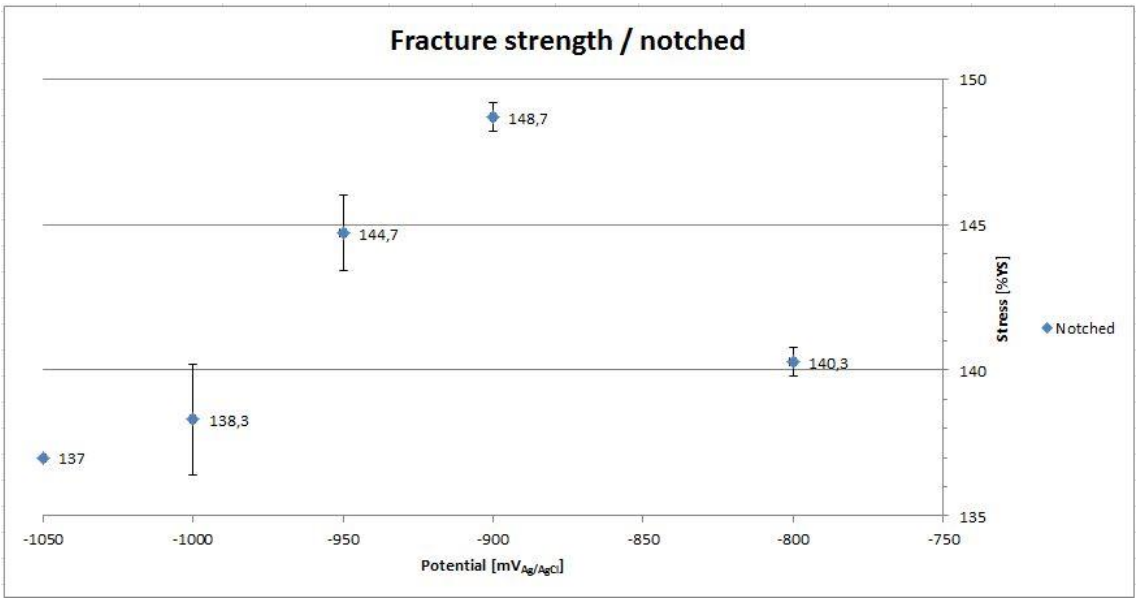

Figure 28 The fracture strength of the notched samples. The values plotted are the maximum stress applied during testing.

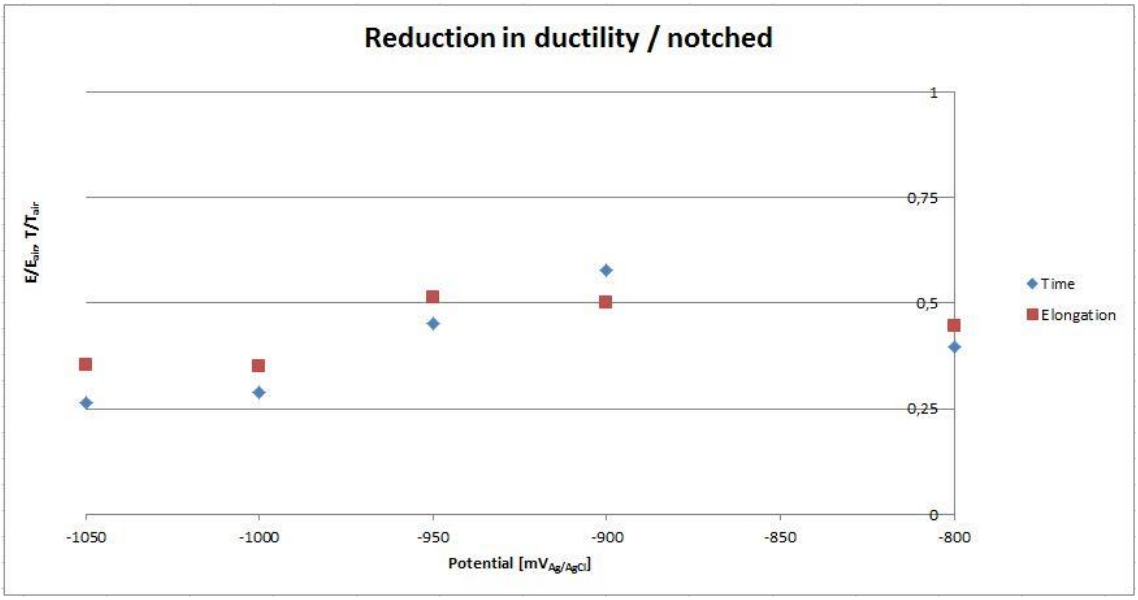

Figure 29 The reduction of ductility measured by both elongation and time. Note that these values were obtained afterwards and should therefore only be used as and indication. The samples fractured at a significantly lower stress than the sample tested in air.

Table 11 lists the fracture stress of the notched samples. Figure 28 shows the maximum load applied during the testing as a plot. Elongation was measured by hand afterwards and is only to be used as an indication, the loss of ductility was also measured by the time to fracture. The ductility results are seen in Figure 29. The notched samples suffered from cold creep, but not in the same order as the non-notched samples. Figure 30 shows a typical stress/time curve for the notched samples, once a critical crack had occurred for these samples the crack was allowed to grow for a certain time until it was wrenched up and fractured. This is seen from 6 hours and outwards in Figure 30. One can also see from comparing Figure 25 with Figure 30 that the creep has been more significant for the non-notched samples.

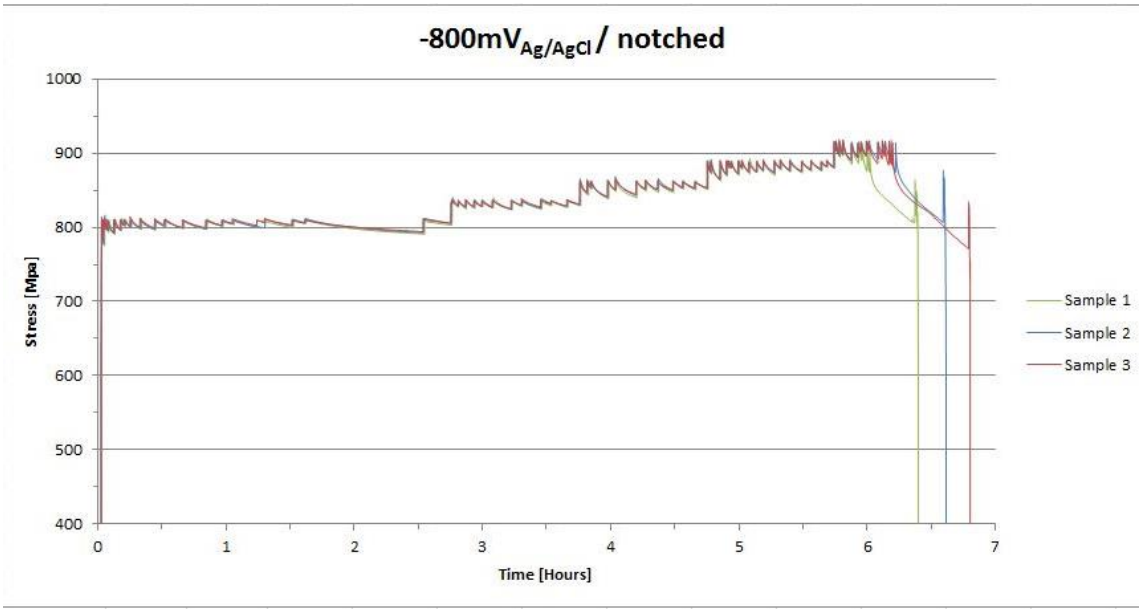

Figure 30 Stress-time graph showing the stress history from the in-situ tensile test of the -800mV$_{Ag/AgCl}$ notched samples. The graph shows a typical result for the in-situ tensile tests, therefore only one graph is included.

There was taken light microscopy photos of all the parallels, all samples fractured from a crack formed in the bottom area of the notch. Figure 31 shows cracks and hydrogen evolution from the -1050mV$_{Ag/AgCl}$ sample 3. These pictures are all taken at the 136% load step, which also were the fracture stress for this sample. It can be noted that the light microscopy showed hydrogen evolution from the backside of the samples at an earlier point, than for the frontside of the samples. There was not taken any good pictures showing this, since it was hard to produce.

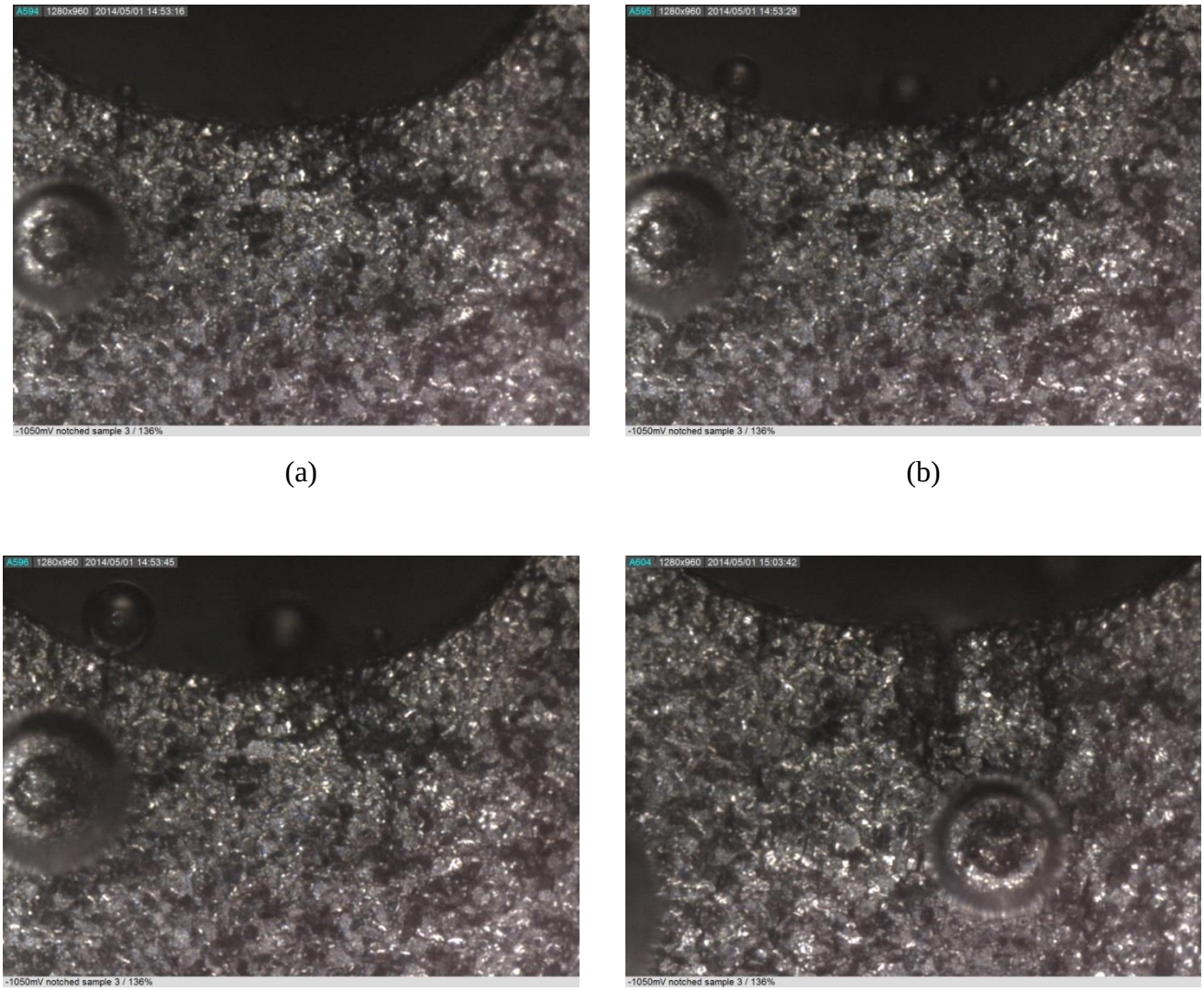

Figure 31 Light microscopy photos from the -1050mV$_{Ag/AgCl}$ sample 3. (a) - (c) is taken within 30 seconds and shows how hydrogen evolves from cracks. (d) is taken at a later point, with more distinct crack growth and small cracks in the nearby areas of the large crack. All the pictures are taken at the 136 % load step.

As done for the non-notched samples, it was also registered when the first cracks where seen in the light microscope. Again this cannot be used as a definite statement for crack initiation, since the resolution of the light microscope setup is limited to around 30µm. It can be noted that cracks was mostly seen at the final fracture stress.

Table 12 Summary of observed crack initiation load for the notched samples. Note that the optical microscope in this setup did not have good enough resolution to detect cracks smaller than around 30µm.

	-1050mV$_{Ag/AgCl}$	**-1000mV$_{Ag/AgCl}$**	**-950mV$_{Ag/AgCl}$**	**-900mV$_{Ag/AgCl}$**	**-800mV$_{Ag/AgCl}$**
Notched	Hydrogen evolution at 132%, suggests cracks. Cracks seen at 136%	First cracks seen at 136%	Crack seen at 144%	Crack seen at 148%	Crack seen at 140%

It was seen that the notched samples showed better sealing of the chambers, due to less elongation during the test. Therefore it was seen less disturbance in the current/potential graphs. This is showed in Figure 32, this was an especially good sample, and not all samples were this stable. Still there is some small noise.

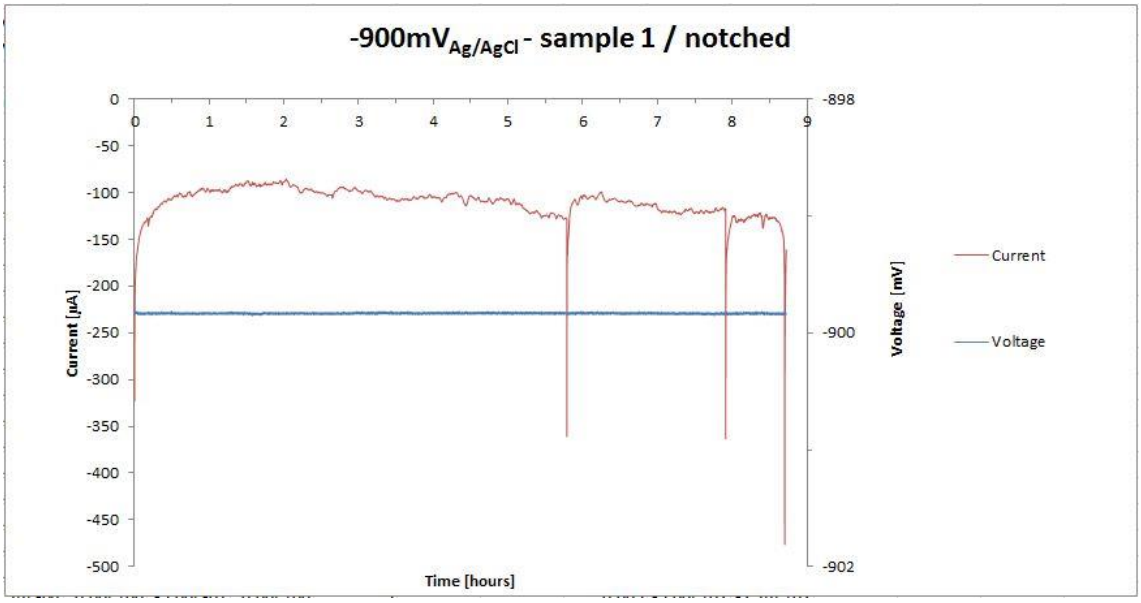

Figure 32 Current/potential graph for the notched -900mV$_{Ag/AgCl}$ sample 1.

4.3 Crack initiation test

There was seen no cracks with the optical light microscope during the testing, but evolution of hydrogen was seen. The graph seen on the computer during the test was inconsistent and hard to read, and the test was stopped at 120% of YS. The current and tensile data can be seen in

Figure 33. The sample was examined for surface cracks in the SEM afterwards, no cracks were found.

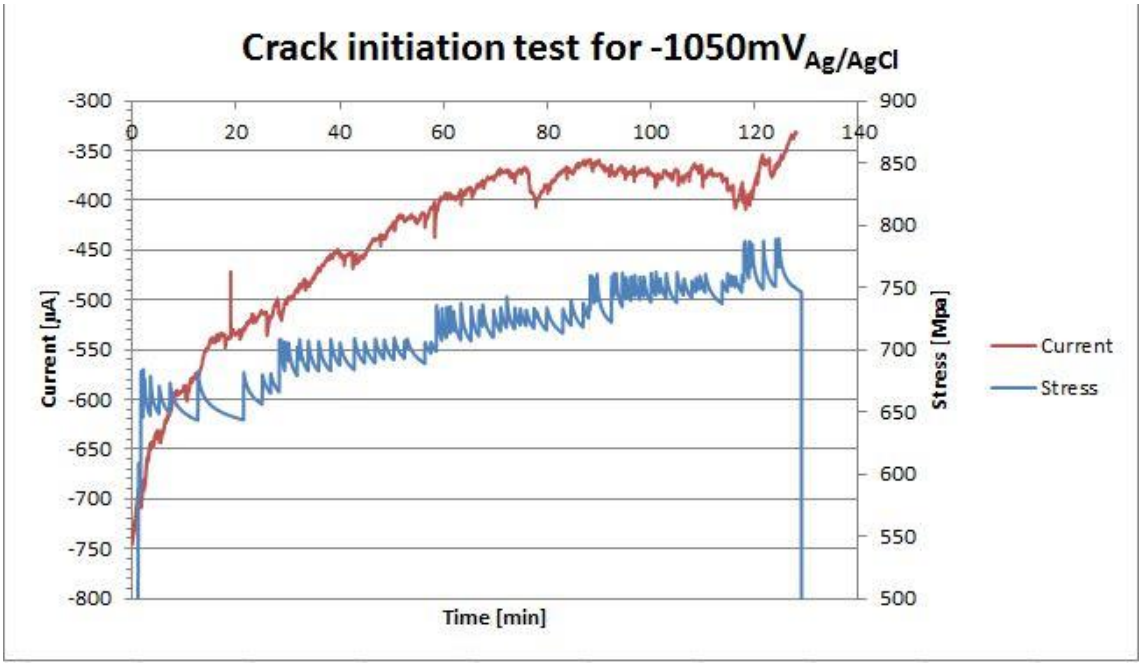

Figure 33 Crack initiation test data.

4.4 Fracture surface analysis

SEM pictures were taken of one sample from each test parallel, the samples were chosen randomly. The non-notched samples that did not fracture were examined for surface cracks, this was also done for the fractured samples. The results from these examinations are listed in Table 13.

4.4.1 Non-notched samples

All of the non-notched samples had surface cracks, in varying size. Table 13 shows the approximate size of the cracks. It can be noted that the cracks decrease in size for more positive potentials.

Table 13 The surface crack/secondary crack size for the different samples, measurements are based on the SEM pictures. Note that few cracks was seen for the notched -900mV$_{Ag/AgCl}$ and -800mV$_{Ag/AgCl}$ samples.

	-1050mV$_{Ag/AgCl}$	**-1000mV$_{Ag/AgCl}$**	**-950mV$_{Ag/AgCl}$**	**-900mV$_{Ag/AgCl}$**	**-800mV$_{Ag/AgCl}$**
Non-notched	70 - 100µm	50 - 90µm	20 - 60µm	10 - 30µm	-
Notched	20 - 500µm	50 - 70µm	20 - 70µm	≈15µm (few)	≈10µm (few)

In Figure 34 surface cracks at the -900mV$_{Ag/AgCl}$ sample is seen. One can see the cracks have propagated through the ferrite grains, and been arrested in the austenite. There are also evident that there are some corrosion on the samples, this was the same for all the non-notched samples by varying character. Only one SEM picture of surface cracks is included, due to the fact that the main difference between the pictures are the crack size.

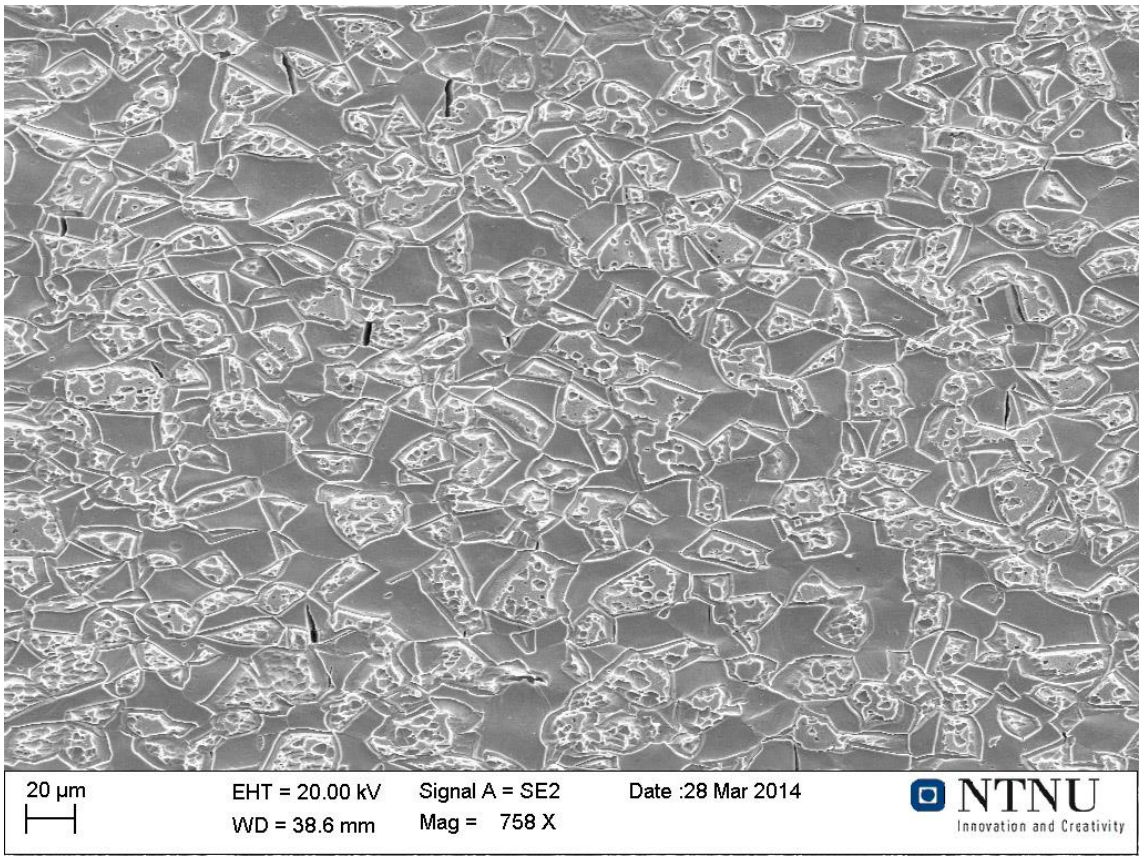

Figure 34 Surface of the -900mV$_{Ag/AgCl}$ sample. Note that the cracks are arrested by the austenite grains.

Figure 35 (a) shows an overview of the -1050mV$_{Ag/AgCl}$ sample 1, brittle fracture features are clearly seen close to the edge. The amount of brittle features decreases towards the centre of the sample, although brittle features were seen throughout the thickness of the sample. The brittle fracture is of type trans-granular or cleavage. Figure 35 (b) – (d) shows the "ductile" area of the top left corner, it is evident that brittle fracture surfaces are seen in this region.

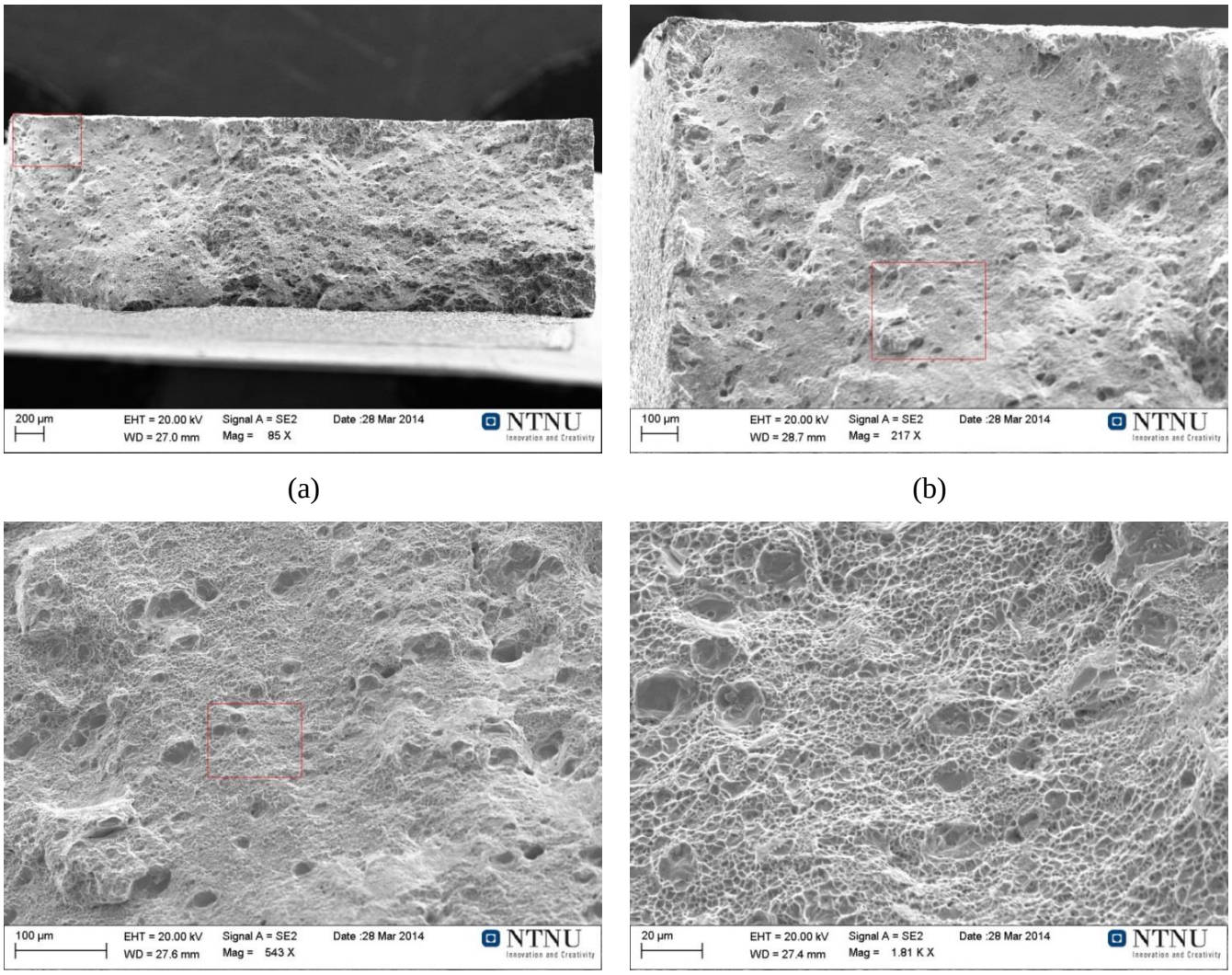

Figure 35 Shows a selection of SEM fractographs from the -1050mV$_{Ag/AgCl}$ sample 1. (a) shows an overview of the sample. (b) – (d) shows the red square at a higher magnification.

4.4.2 Notched samples

All of the fractured samples were examined in the SEM, in addition the surfaces of the samples were investigated in the SEM. The results from the surface analysis are listed in Table 13. The SEM pictures are of the same appearances as for the non-notched samples. Corrosion was also seen here in varying amount. The most unstable pre-charged samples had most corrosion, while for the -800mVAg/AgCl sample no corrosion was present. A difference between the non-notched and notched samples that can be noted, is that the amount of cracks was significantly less on the notched samples. If Figure 34 is compared to Figure 36, this is clearly evident. Since hydrogen evolution was seen at an earlier point from the back side of

the samples, the -800mV$_{Ag/AgCl}$ and -900mV$_{Ag/AgCl}$ samples were examined on the back side as well, no major differences were seen.

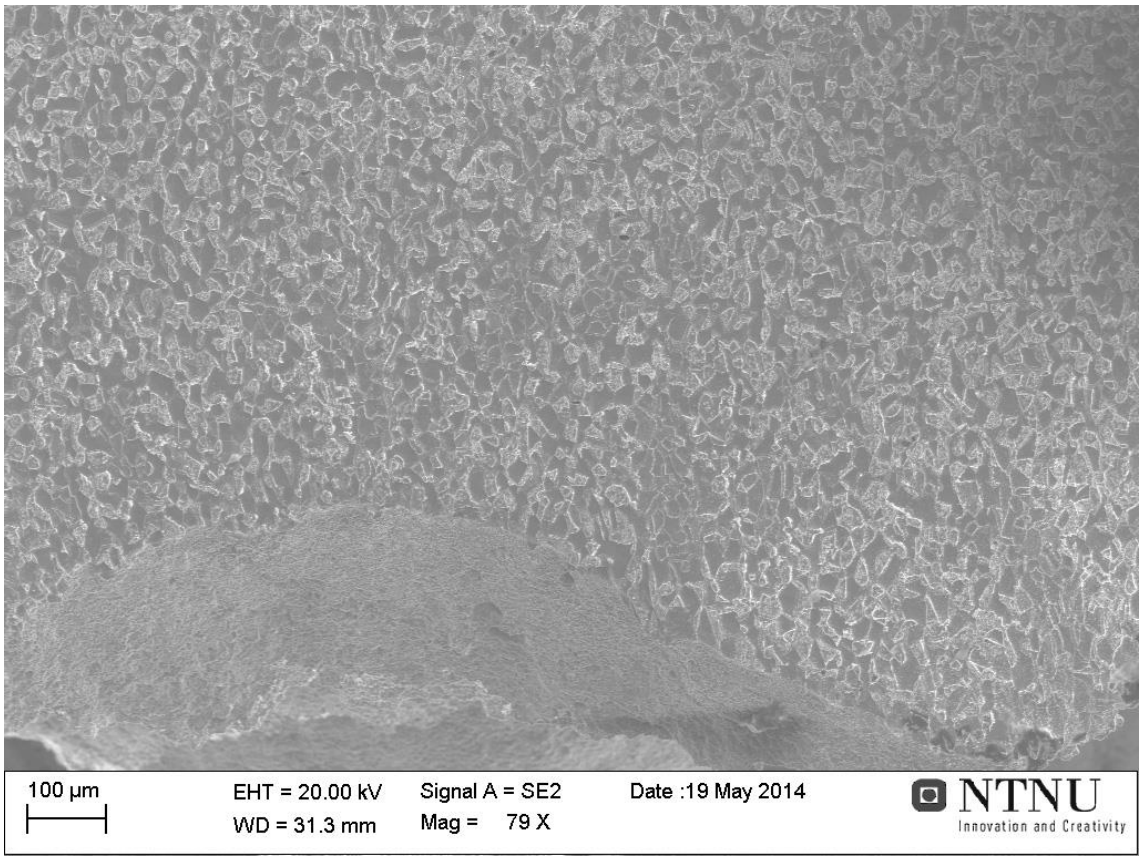

Figure 36 Surface of the notched -900mV$_{Ag/AgCl}$ sample. One small crack is seen in the centre of the figure.

Figure 37 shows an overview of all the samples. From this one can see the degree of embrittlement the different potentials have caused. One can see a trend for less embrittlement for more positive potentials. The -1050mV$_{Ag/AgCl}$ sample was embrittled all the way through to the centre of the sample, this is shown in Figure 38, where both brittle and ductile fracture feature features are seen. Figure 39 shows the centre of the -1000mV$_{Ag/AgCl}$ sample, compared to the -1050mV$_{Ag/AgCl}$ sample less embrittlement is evident, but still there are some brittle fracture features. More pictures of the fracture surfaces are listed in Appendix A.

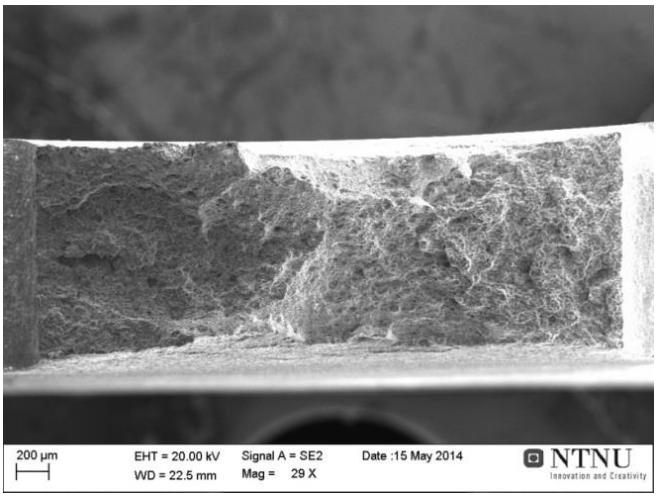

(a)

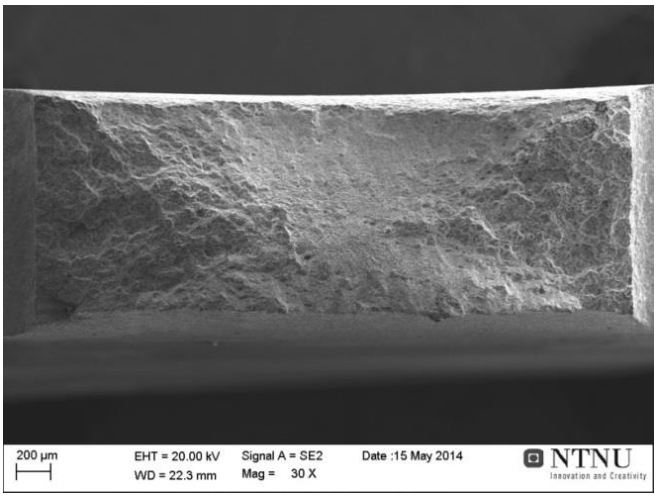

(b)

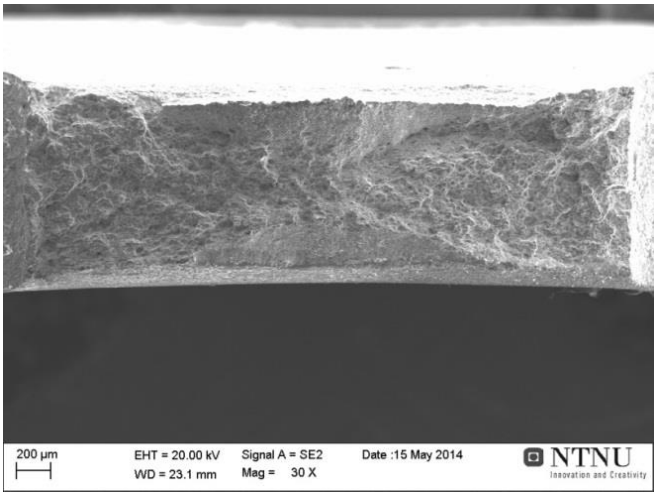

(c)

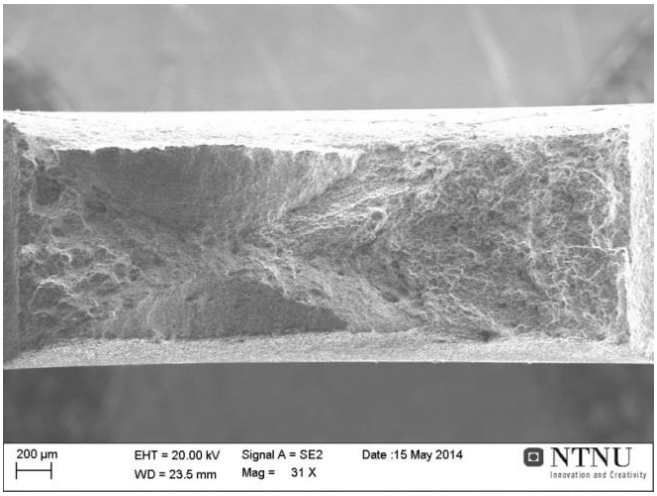

(d)

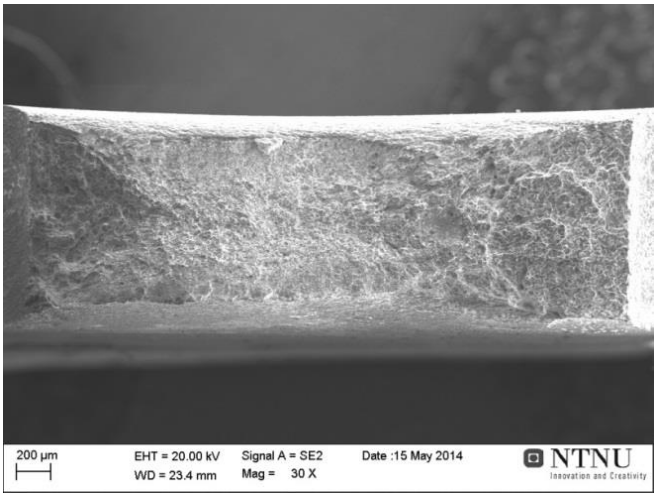

(e)

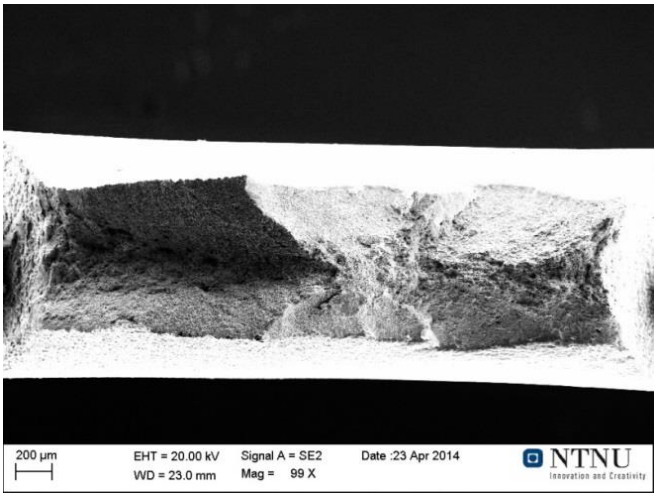

(f)

Figure 37 Shows an overview of the fracture surfaces of the notched samples. From -1050mV$_{Ag/AgCl}$ to in air, from (a) - (f) respectively.

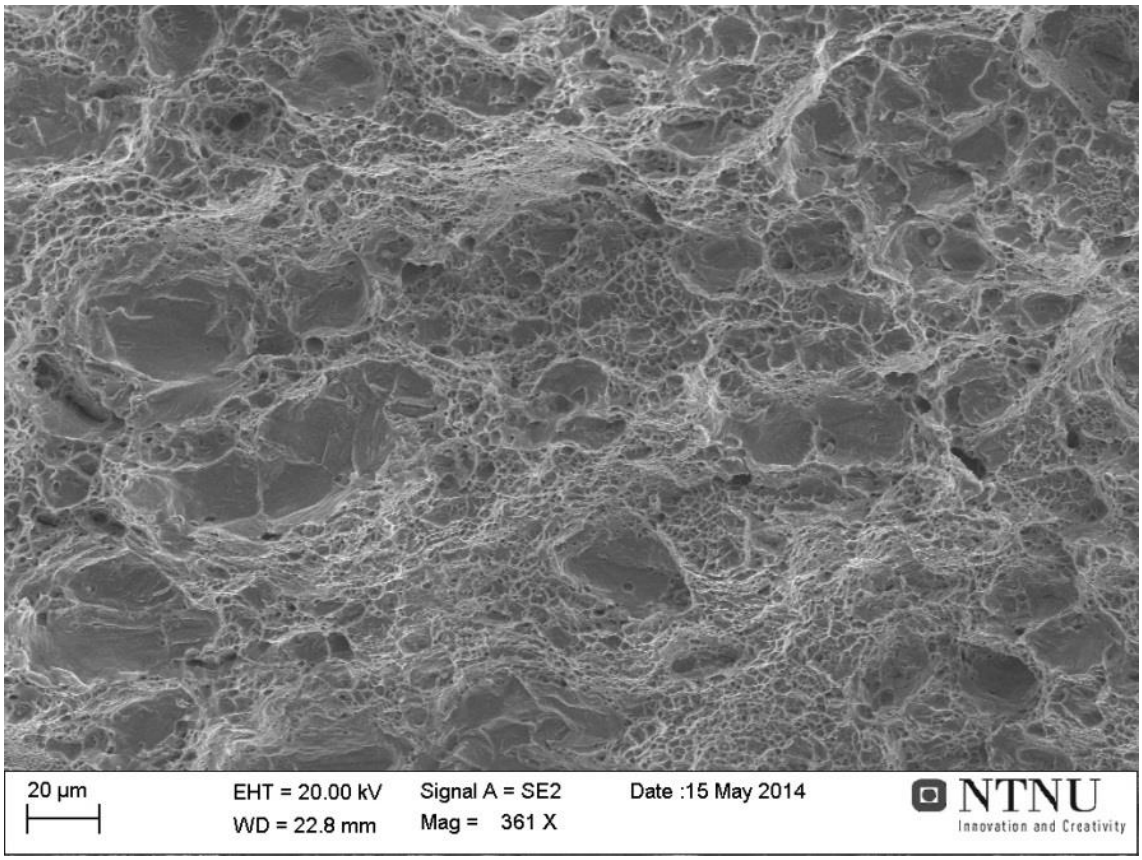

(a)

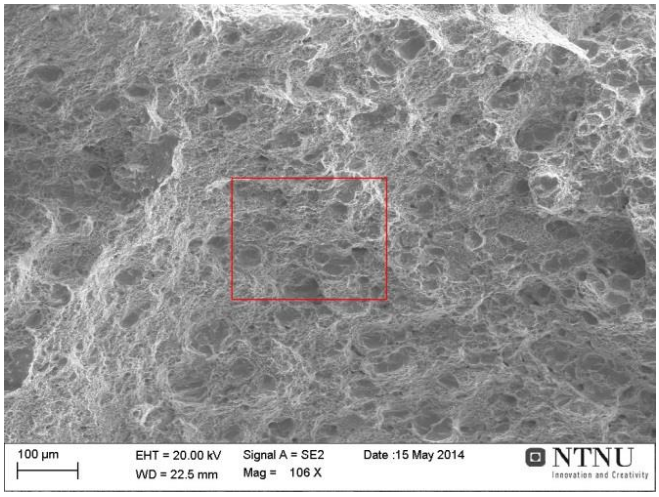

(b)

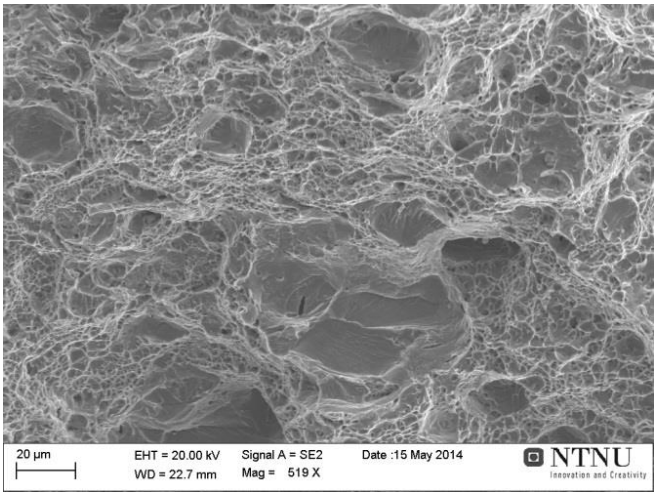

(c)

Figure 38 From the centre of the -1050mV$_{Ag/AgCl}$ sample. (a) is taken from a different location than (b) and (c). (c) is the red square from (b) at a higher magnification level.

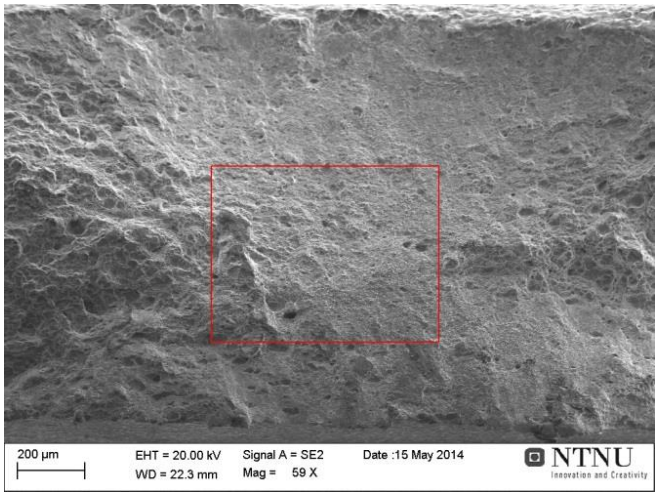

(a)

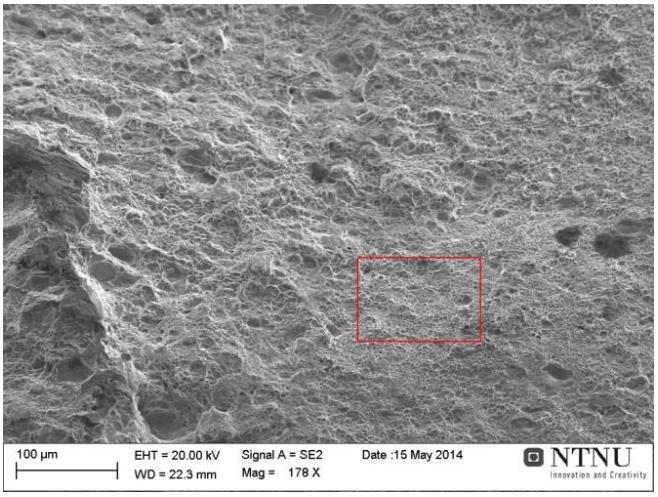

(b)

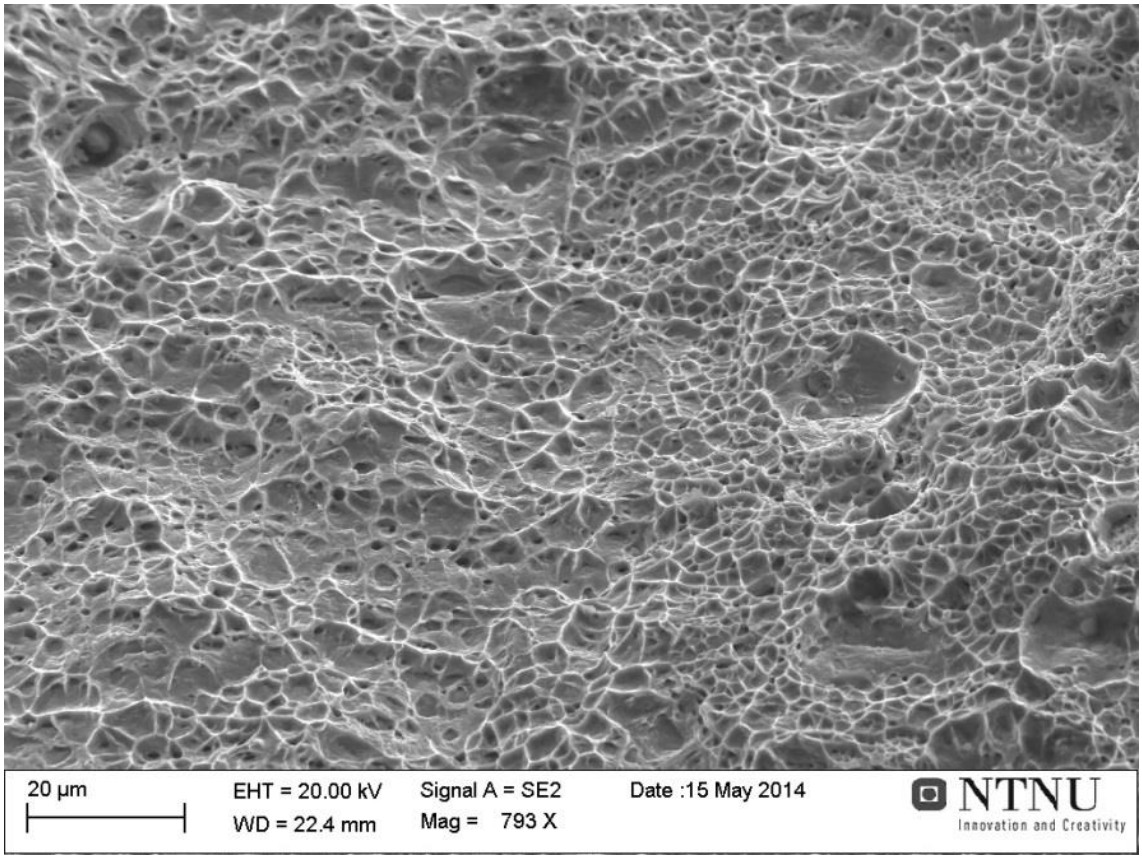

(c)

Figure 39 The centre of the -1000mV$_{Ag/AgCl}$ sample. (b) and (c) are higher magnification pictures of the area marked by the red square in (a) and (b), respectively.

.

4.5 Hydrogen measurements

The results from the hydrogen measurements can be seen in Figure 40. It can be noted that there are no consistency between the different potentials and the highest hydrogen content is found in the -800m$V_{Ag/AgCl}$ sample, opposite to what was expected. The accuracy of the results is in the order of 0.001 ppm.

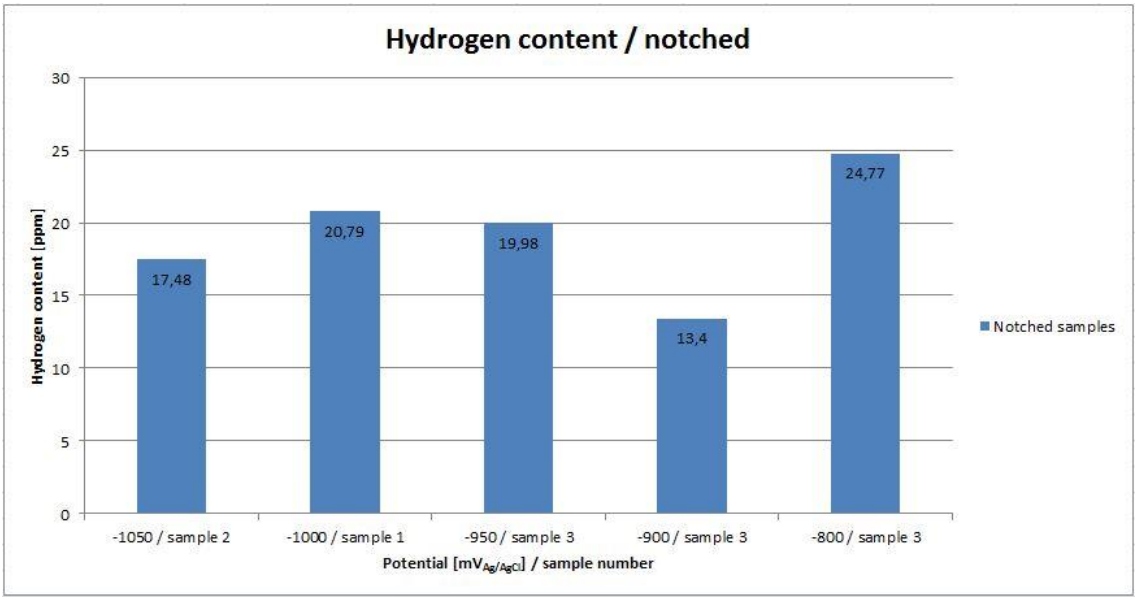

Figure 40 Hydrogen content for the notched samples. The measurements were only done on one of the samples, indicated in the plot.

5 Discussion

To establish a good frame for discussing the results obtained in this work, it is necessary to start with the sample preparation and pre-charging setup and it's positive and negative sides.

5.1 Sample preparation and pre-charging setup

The sample preparation in this work was the same as for the project work done during the fall semester. The pre-charging setup was an updated version from the same project work.

5.1.1 Sample preparation

The samples were thoroughly polished and the front side was electropolished. Due to the fact that hydrogen evolution was seen first from the backside of the samples and the fact that when cracks had formed hydrogen evolved steadily from these cracks, from this one could argue that cracks formed at an earlier stage on the not electropolished back side of the samples. This also gives sense in the way that with a rougher surface, there will be a higher amount of stress intensifying locations throughout the samples surface. But since the back side was polished at 1μm this would give an almost as smooth surface as the electropolished front side. Another reason for earlier hydrogen evolution on the back side could be the fact that the platinum wire is located on the backside of the sample and are in no visual contact to the front of the sample, therefore the current density would be higher on the back side, giving higher hydrogen evolution. When looking at both sides in the SEM there were not seen any big differences between the sides. It is difficult to conclude on the reason(s) for the higher hydrogen evolution from the back side, but it is believed that the higher current density plays a major role.

5.1.2 Pre-charging setup

The new pre-charging setup enabled the samples to be pre-charged at a significantly higher temperature, which lead to a higher hydrogen content over a shorter time period than possible in the foregoing project work. Some of the samples had corrosion on them, which should in the theory not be possible, since they were protected with CP at all times. But seeing the current/potential graphs from the pre-charging, Figure 23 and Figure 24, this was not the case. The pre-charging was not stable. Compared with the pre-charging done with 3.5% NaCl solution in the foregoing project work, that setup showed a higher degree of stability. Reasons for the setup not being stable can be many, the present electrolyte has a higher resistance and therefore more current is needed to reach the lowest potentials. It was also more difficult to

control the electrolyte level in the reference electrode container, but this was more a matter of operator experience. Due to limited work space, the pre-charge setup was placed a distance away from the potensiostats, thus needing a high amount of cables to connect the pre-charge to the potensiostat. If done again, this distance should be minimized. When changing electrolyte the setup is disturbed and contributes to unstable operation. When the electrolyte blackened the integrity of the electrolyte may be not as complete as it should and this might contribute to unstable operation. When looking at the average current for the different pre-charging setups one can see that the current is roughly more negative for the more negative potentials, but due to the unstable nature of the curves it is hard to state definitely. A more negative potential giving a more negative current is in line with electrochemical theory. Too conclude if it is recommended to use this new setup is difficult, but due to the electrolyte being more aggressive than 3.5% NaCl solution, an unstable pre-charging will have more severe consequences, i.e. higher risk of corroded samples. And it is thought that this is the reason for the corrosion seen on the samples.

Regarding the hydrogen content, it was seen that there were no consistency between potential and hydrogen content. There was neither any consistency between average pre-charging current and hydrogen content. A reason for this could be that the unstable pre-charging led to this, one could note that the highest hydrogen content was found for the -800m$V_{Ag/AgCl}$ sample. In theory this should be the sample with the lowest hydrogen content, but from the pre-charging graph it is seen that this was the most stable pre-charge. One could question whether the present electrolyte alters the potential for hydrogen evolution compared to 3.5% NaCl electrolyte, since -800m$V_{Ag/AgCl}$ has seen to be a “safe” potential in an earlier work by Chang et al, but they used an pre-charge in RT over 30 days in artificial sea water resulting in average hydrogen content for a -850m$V_{Ag/AgCl}$ sample to be below 4ppm, and giving the -800m$V_{Ag/AgCl}$ sample had the highest hydrogen content off all this could be discussed. Another view is that this earlier work did not pre-charge at such a high temperature, this temperature would give a much higher hydrogen uptake, due to increased diffusion, and also higher hydrogen evolution will be seen because of the increase in kinetics when increasing the temperature. This could have enabled a higher hydrogen uptake, and thus simulating the hydrogen content in a component after a longer time of operation better, than this earlier study could have done. Thus it would be reasonable to say that the electrolyte represents the hydrogen evolution for salt water in a satisfactory way. The drawback for the new electrolyte

is the unstable operation, and therefore it might be a better solution to use a 3.5% NaCl electrolyte and pre-charge at a longer time.

5.2 In-situ tensile test

Both the non-notched and notched samples gave in general reasonable results, with the notched samples having an unexpected increase in HISC resistance for the -800m$V_{Ag/AgCl}$ samples. The tests themselves went according to the plan, with some minor differences with sealing of the chambers, this is as expected as it is hard to ensure good sealing with the current chamber design. It is noted two stress values in the results chapter, the fracture stress and the maximum reached stress. It is decided to use the fracture stress values, since the maximum stress has only been held for a short time, and it is stated for HISC to occur the stress has to be held over a couple of minutes.

5.2.1 Non-notched samples

For the non-notched samples only the -1050m$V_{Ag/AgCl}$ samples went to fracture, the fracture strength was 136±0% of YS. Because of this another set of test were conducted, but now with a notch. The load step reached varied within each test parallel and between the potentials. The reason for this is due to different creep adjustment from sample to sample. The creep adjustment was done by hand, and it was hard to ensure that the samples were adjusted for at the same intervals. This led to the samples reaching different load steps and it is not believed that the results says anything more about HISC susceptibility than the maximum load step they reached and any differences between them could not be commented on, since only one of them went to fracture. It was taken SEM pictures of all the surfaces and here it was seen clear differences between the different potentials. As expected the more negative potential, a higher degree of HISC was seen. This was seen as the surface cracks were bigger for the more negative potentials, it was seen a good consistence between crack size and potential. This is according to the theory of higher hydrogen content will give a higher degree of embrittlement, and therefore suggests that the hydrogen content is highest for the most negative potential, this was not the case for the notched samples. The fractograph of the -1050m$V_{Ag/AgCl}$ sample brittle fracture features were clearly seen, the corners did see whole areas of cleavage fracture and in the centre of the sample it was mostly dimples, indicating ductile fracture, but it was also here seen small areas of cleavage fracture. This indicates that hydrogen has diffused into the centre of the sample. Since there was not taken any hydrogen measurements of the non-notched samples, no evaluation regarding hydrogen content will be possible.

5.2.2 Notched samples

All of the notched samples fractured, giving a good set of results to discuss HISC susceptibility of the current material. It was seen that the -1050m$V_{Ag/AgCl}$ samples showed the lowest facture strength of 136±0% of YS, but the fracture strength of the -1000m$V_{Ag/AgCl}$ samples, 137.3±1.9% of YS, was in the same region as the -1050m$V_{Ag/AgCl}$ samples and it could be argued that this is only a normal discrepancy. It was also seen that the -800m$V_{Ag/AgCl}$ samples fractured within this area as well (140% of YS). The -950m$V_{Ag/AgCl}$ samples and especially the -900m$V_{Ag/AgCl}$ samples fractured at higher loads than the other samples, respectively 144±0%- and 148±0% of YS. It was not expected to see the -800m$V_{Ag/AgCl}$ samples having higher fracture strength than these two samples. The hydrogen measurements are helpful to explain the reasons for these results, but did not give any conclusive and clear answers. It was seen that the hydrogen content was highest for the -800m$V_{Ag/AgCl}$ and second lowest for the -1050m$V_{Ag/AgCl}$ samples, which showed the lowest fracture strength. The hydrogen content for the -900m$V_{Ag/AgCl}$ samples were the lowest, this gives indications to explain why this set of samples showed the highest fracture strength. Explaining the fracture strength for the -950m$V_{Ag/AgCl}$ samples are not as straight forward, one explanation could be the fact that both the -950m$V_{Ag/AgCl}$ samples and the -900m$V_{Ag/AgCl}$ samples both stood six hours at 120°C without any protection potential, thus enabling hydrogen diffusion outwards. From using the thick plate solution of Fick's 2nd law, seen in Figure 41, it is obvious that there will be a higher hydrogen concentration close to the surface of the sample. The hydrogen measurements taken here are only an average value and therefore in general all samples will have a higher surface concentration. As mentioned the -950m$V_{Ag/AgCl}$ and -900m$V_{Ag/AgCl}$ stood six hours without any potential, thus surface hydrogen would start diffusing outwards and lowering the surface content. Therefore it is believed that the surface concentration of hydrogen for these two samples is lower than for the rest of the samples. On can note that for future reference it would be wise to make sure the samples do not stay unprotected at the end of a pre-charge.

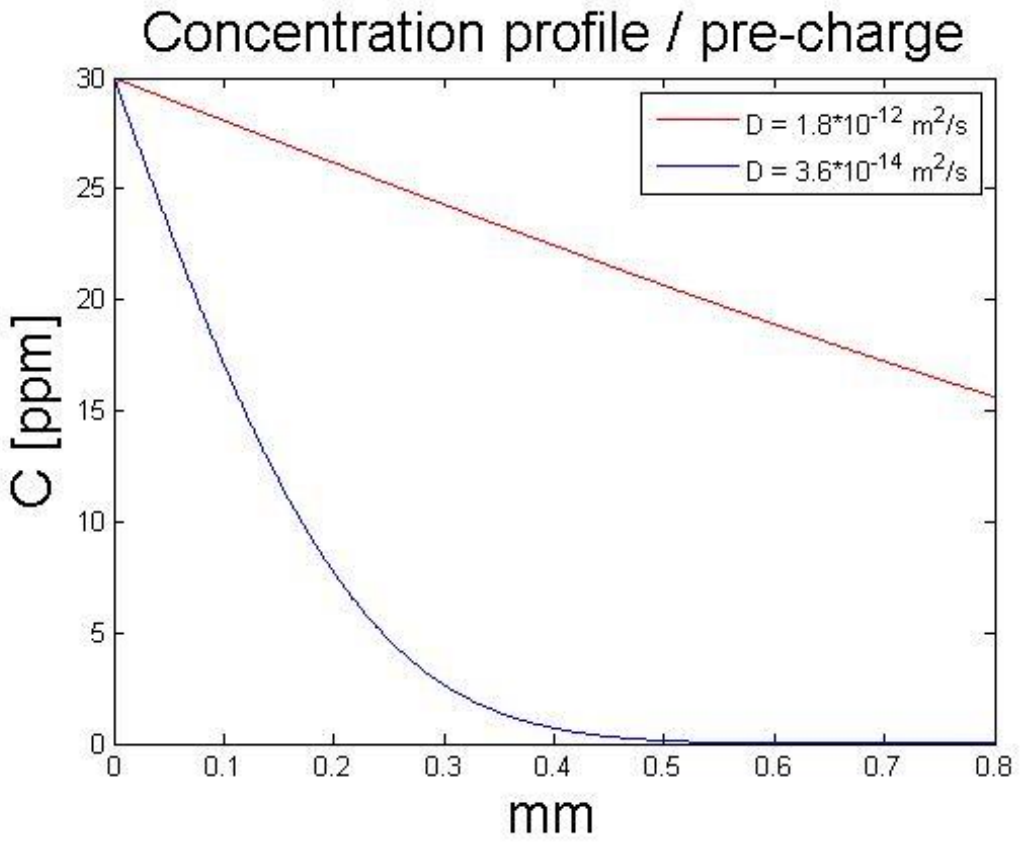

Figure 41 Thick plate solution of Fick's 2nd law. The diffusion coeficients are taken from section 2.5.1, and the surface concentration is chosen only to illustrate the profile, and does not have any scientific arguement behind itself. The MatLab script used is found in Appendix B.

This can help explaining the results, during pre-charging hydrogen would be trapped at both reversible traps and irreversible traps. When hydrogen was allowed to diffuse out of the samples, un-trapped and reversible trapped hydrogen would diffuse, while the measured hydrogen could be mostly irreversible trapped hydrogen that could not diffuse to high stress fields and further embrittle and contribute to lower fracture strength. In addition the outer part of the sample will most likely have significantly lower hydrogen content than the centre of the sample, giving a low "hydrogen supply" to surface cracks and defects, and thus resulting in higher fracture strength. In addition the low hydrogen content of the -900m$V_{Ag/AgCl}$ samples could be because of the unstable pre-charge seen for these samples in combination with the last six hours at 120°C without protection.

5.2.3 HISC results

All of the samples, including the fractured non-notched -1050m$V_{Ag/AgCl}$ sample showed a very high resistance to HISC. Seeing the lowest fracture strength of 136% of YS is a high value. Compared to Andersen's work, where the fracture strength of the same material was found to be 123±5.6% of YS, this is significantly lower than for the present work. For the foregoing

project work the fracture strength was found to be 130±2% of YS. For both of these earlier works the test procedure was done over a longer time period, in addition Anderson's samples were not polished, as in this work. When the surfaces of the samples are smoother, there are less stress intensifiers and this may contribute to a higher fracture load for the smooth samples. Increasing the time period for the test, will allow for hydrogen to diffuse towards the surrounding stress field of a defect or crack. This may allow for higher crack growth at lower stress levels, and thus lowering the fracture strength. The reason for the higher fracture strength seen in the present work, compared to the results from the foregoing project work is believed to be of the shorter time frame the current tests were done at. Therefore if a test shall reveal true fracture stress for components in operation, it is thought that adequately pre-charged samples should be constant load tested with a significantly large time frame. Both Kivisäkk and Ronneteg et al. reported that no surface cracks were seen at a load of 130% of YS for a SDSS with similar austenite spacing as the material tested here. From the light microscope pictures it was seen that the first cracks was seen at 132% of YS, and most samples did not see cracks until a higher load step was reached. This is in line with the results Kivisäkk and Ronneteg et. al found. It should be noted that cracks smaller than 30µm was not detected by the light microscope, and therefore the results are not 100% thrust worthy. But it is believed that cracks did not form on a significantly lower stress level, and therefore the results are in accordance to what Kivisäkk and Ronneteg et. al found. For the notched samples there was taken measurements trying to quantify the reduction in ductility. They showed a significantly loss of ductility compared to the sample tested in air, this is a clear sign of HISC and confirms that the fracture values indicates HISC.

The notched -1050mV$_{Ag/AgCl}$ showed the same fracture strength as the non-notched -1050mV$_{Ag/AgCl}$ samples. It could have been expected that the notched samples fractured at a slightly lower stress level. This is because a notch could introduce a very high stress concentration leading to a slightly lower fracture stress. It is believed that for the notch implemented in this study, the bottom of the notch was not sharp enough, tip radius of 0.3mm, to provide such a high stress concentration and therefore resulting in the same fracture stress as the non-notched samples.

When comparing the results from the different potentials it is seen that all samples suffered from HISC. This is seen clearly by seeing the fracture stress being lowered from 161% of YS to 148% of YS for the least HISC affected samples, the -900mV$_{Ag/AgCl}$. The high fracture stress for the sample tested in air, when looking at the material data the UTS is given as 136%

of YS, is believed to be an effect of the sample preparation giving an extremely smooth surface. When comparing an UTS of 136% of YS it is not evident that the samples suffered from HISC, but the result from the sample tested in air is used as a guideline and not the given UTS. It was seen an increasing HISC resistance for more positive protection potential, except for the -800mV$_{Ag/AgCl}$ sample. This proved that -800mV$_{Ag/AgCl}$ is not a safe potential for escaping HISC risk. This was also shown by the hydrogen measurements, showing the highest hydrogen content. The hydrogen content will be further discussed. The differences between the different potentials, was as mentioned an increase in fracture strength with increasingly more positive potential, except for the -800mV$_{Ag/AgCl}$ samples as briefly discussed earlier. Taking the -800mV$_{Ag/AgCl}$ samples had the highest hydrogen content, it is believed that the role the potential plays is altering the time frame for HISC to occur. This is suggested based on the evaluating the un-stable pre-charge results. With a more positive potential, the time to HISC risk will be increased. Off course, when CP is applied it will only be a risk as long as the potential is adequately negative for hydrogen evolution to take place. This will all ways be the case when CP is applied, since the protection potential for carbon steel is stated to be -800mV$_{Ag/AgCl}$. The hydrogen measurements are not in complete compliance with this theory, because of the varying hydrogen contents. But the unexpected spread of the hydrogen content is believed to be of the pre-charge results, and therefore the suggested theory seems likely.

5.3 Crack initiation test

The crack initiation test did not give any usable results, the test setup were seen not to give a stable current. And therefore it was difficult to look for current drops indicating crack formation. In addition when the light microscope has a limitation of around 30µm, this cannot be used to detect the cracks either. The current is believed not to be stable because of some various factors, such as the hydrogen formation results in bubbles sticking to the sample surfaces, altering the surface area in contact with the electrolyte. When the bubbles escape the surfaces, it will upset the nearby electrolyte and introduce flow in the electrolyte. When the chamber start leaking and it is necessary to fill it up again, this will greatly disturb the current. In some cases there will only be small leaks, so there will not be necessary to fill up the chamber, although this will increase the area of the sample in contact with electrolyte and therefore upset the current. Due to this it is not seen fit to run a crack initiation test for the current setup. If using the electrolyte used in the pre-charge, 2:1 glycerol – H_3PO_4, this could

give a more stable current, since the electrolyte is more viscous, and many of the issues listed above would possibly be eliminated.

5.4 Fractographs

The fractographs have been briefly commented on in the results chapter. In this section they will be further commented on and discussed. From the tensile test results, as mentioned, it was seen that the fracture strength was increased with a more positive potential, except the -800m$V_{Ag/AgCl}$. The hydrogen measurements gave no certain trends, but the overview SEM fractographs and when looking at higher magnifications of the different samples it was clear that the amount of brittle fracture character decreased with increasingly positive potential. Seen in the light of the hydrogen measurements and the tensile test data, one would expect the -800m$V_{Ag/AgCl}$ fractographs to show more brittle character than both the -950m$V_{Ag/AgCl}$ and the -900m$V_{Ag/AgCl}$, but this was not the case. Explaining these results could be done by the same argument as used above in section 5.2.2. Since the -950m$V_{Ag/AgCl}$ samples and the -900m$V_{Ag/AgCl}$ stood the last six hours at 120°C without any protection potential, this could have contributed to most of the hydrogen at the surface diffusing out of the sample. Therefore less hydrogen could have diffused to areas with high hydrostatic pressure at the surface, such as defects and stress risers, and embrittled them. Leading to higher fracture strength, but still with a significant hydrogen amount in the centre of the sample, which could be reversible or irreversible trapped, giving the relative high amount of brittle fracture characteristics. This cannot be confirmed with the experimental test done in this work. A hydrogen profile could have given light to this argument and given answers to this question.

5.5 Hydrogen measurements

The hydrogen measurements were not as one could expect from an electrochemical view, since a more negative potential should give a higher hydrogen evolution. Reasons for the results have been briefly discussed in the earlier sections of this discussion. But it is thought to be wise to summarize and further discussed these different theories here. Exceptions from the expected results where the hydrogen content for the -1050m$V_{Ag/AgCl}$ sample being the second lowest value, and that the -800m$V_{Ag/AgCl}$ sample giving the highest hydrogen content of all the samples. To try to understand this it is important to look at the pre-charging results, as it is reasonable to believe that most the hydrogen are coming from here. The contribution from the tensile test is most likely very small compared to the pre-charge, due to the fact that it is done at room temperature and not at 120°C. From the graphs one can see that the -

800mV$_{Ag/AgCl}$ samples has been the most stable and compared to the -1050mV$_{Ag/AgCl}$ samples where rather unstable and even had a ten hour period without any protection potential, this occurred because of losing the reference electrode. The -900mV$_{Ag/AgCl}$ sample showed the lowest hydrogen content, the pre-charge was unstable and in addition the samples stood six hours after the pre-charge without any potential, this was due to the computer updating during night. It should be mentioned that the measured hydrogen contents are all fairly similar, with few large deviations, as mentioned earlier. From the results two conclusions can be proposed. All the tested potentials are giving similar hydrogen content ant it could be argued that the samples are close to the saturation point. Chang et. al reported that a similar DSS showed saturation at 12 – 16ppm on the other hand Andersen reported a hydrogen content for the same material used her to be 91.5 and 132.8ppm, therefore saturation of the samples is not believed to have occurred. The second notion that could be made is that the pre-charge is essential, in the way of stability, for getting good and consistent hydrogen contents.

5.6 Further work

To further investigate the HISC behaviour of SDSS in the light of different potentials, it would be interesting to run tests at a longer time frame to ensure more of an operational like environment. In addition constant load test run at different stress levels or to run the test with strain as a parameter, this would make the test easier to maintain. Because of the need to adjust for creep would not be an issue, this would also make it easier to replicate the test. In regards of hydrogen measurements, it would be strongly recommended to do measurements which could give a hydrogen profile as output data. This could be done with for example Secondary Ion Mass Spectrometry (SIMS). It could also be interesting to look into the hydrogen saturation level for the given SDSS.

6 Conclusion

In-situ tensile testing of Super Duplex Stainless Steel pre-charged at different potentials has been conducted. The SDSS had an austenite spacing of 12.9µm, have been pre-charged in a 2:1 glycerol – H_3PO_4 electrolyte and in-situ tensile tested in 3.5% NaCl electrolyte. Non-notched- and notched samples have been tested. All of the samples have been investigated in the SEM for surface/secondary cracks and the fractured samples have been taken fractographs of. From the notched samples it was taken hydrogen measurements of one sample from each test parallel.

All tested samples showed low temperature creep, with the notched samples showing significantly less creep than the non-notched. HISC was evident for all samples, to which extent the samples suffered from HISC were varying. For the non-notched samples the -1050m$V_{Ag/AgCl}$ samples fractured at 136±0% of YS, the other samples pre-charged at more positive potentials were to ductile for the test setup. Surface cracks where seen on all samples, there were clearly seen a trend of larger cracks for more negative potentials. The notched samples were pre-charged at -1050m$V_{Ag/AgCl}$, -1000m$V_{Ag/AgCl}$, -950m$V_{Ag/AgCl}$, -900m$V_{Ag/AgCl}$ and -800m$V_{Ag/AgCl}$ and fractured at 136±0%, 137.3±1.9%, 144±0%, 148±0% and 140±0% of YS respectively. A sample tested in air fractured at 161% of YS. Surface/secondary cracks were seen on all samples and the same trend was seen as for the non-notched samples. The tested material showed good resistance to HISC.

Hydrogen content varied from 13.40ppm to 24.77ppm. At -800m$V_{Ag/AgCl}$ the samples suffered from HISC and therefore it is concluded that this is not a safe potential regarding HISC failure. It was seen that a hydrogen content of 13.40ppm was sufficient to promote HISC, and higher hydrogen content gave a more severe HISC attack.

References

1. Woollin, P. and A. Gregori. *Avoiding hydrogen embrittlement stress cracking of ferritic austenitic stainless steels under cathodic protection*. 2004. ASME.
2. Andersen, K., *HISC in Super Duplex Stainless Steels*, in *IMTE*. 2013, NTNU: Trondheim.
3. Cassagne, T. and F. Busschaert, *A review on hydrogen embrittlement of duplex stainless steels*, in *CORROSION 2005*. 2005: Houston, Texas.
4. Nisancioglu, K., *Corrosion basics and engineering.*
5. Veritas, D.N., *DNV-RP-B401*.
6. Johnsen, R., et al., *New improved method for HISC testing of stainless steels under cathodic protection*, in *CORROSION 2007*. 2007: Nashville, Tennessee.
7. Mehrer, P.D.H., *Diffusion of Interstitial Solutes in Metals*, in *Diffusion in Solids*. 2007, Springer Berlin Heidelberg. p. 313-326.
8. Kumar, P. and R. Balasubramaniam, *Determination of hydrogen diffusivity in austenitic stainless steels by subscale microhardness profiling.* Journal of Alloys and Compounds, 1997. **255**(1–2): p. 130-134.
9. Brauser, S. and T. Kannengiesser, *Hydrogen absorption of different welded duplex steels.* International Journal of Hydrogen Energy, 2010. **35**(9): p. 4368-4374.
10. Owczarek, E. and T. Zakroczymski, *Hydrogen transport in a duplex stainless steel.* Acta materialia, 2000. **48**(12): p. 3059-3070.
11. Zakroczymski, T. and E. Owczarek, *Electrochemical investigation of hydrogen absorption in a duplex stainless steel.* Acta materialia, 2002. **50**(10): p. 2701-2713.
12. Shewmon, P., *Diffusion in Solids*. 2nd ed. 1989, Pennsylvania: The Minerals, Metals & Materials Society.
13. Olden, V., *FE modelling of hydrogen induced stress cracking in 25% Cr Super Duplex Stainless Steel*". 2008, Norwegian University of Science and Technology: Trondheim.
14. Olden, V., C. Thaulow, and R. Johnsen, *Modelling of hydrogen diffusion and hydrogen induced cracking in supermartensitic and duplex stainless steels.* Materials & design, 2008. **29**(10): p. 1934-1948.
15. Olden, V., et al., *Influence of hydrogen from cathodic protection on the fracture susceptibility of 25%Cr duplex stainless steel – Constant load SENT testing and FE-modelling using hydrogen influenced cohesive zone elements.* Engineering Fracture Mechanics, 2009. **76**(7): p. 827-844.
16. Oriani, R.A., *The diffusion and trapping of hydrogen in steel.* Acta Metallurgica, 1970. **18**(1): p. 147-157.
17. DNV, *DNV-RP-F112*. 2008.
18. Lauvstad, G., et al., *Resistance Toward Hydrogen-Induced Stress Cracking of Hot Isostatically Pressed Duplex Stainless Steels Under Cathodic Protection.* Corrosion, 2010. **66**(11): p. 115004-115004-13.
19. Olden, V., *FE modelling of hydrogen induced stress cracking in 25 % Cr duplex stainless steel*, in *Department of Engineering Design and Materials*. 2008, Norwegian University of Science and Technology: Trondheim.
20. Dieter, G.E., *Mechanical Metallurgy*. 3rd ed. 1961, London: McGraw-Hill Book Company.
21. Chen, S.S., T.I. Wu, and J.K. Wu, *Effects of deformation on hydrogen degradation in a duplex stainless steel.* Journal of Materials Science, 2004. **39**(1): p. 67-71.
22. Anderson, T.L., *Fracture Mechanics: Fundamentals and Applications, Third Edition*. 2005: Taylor & Francis.
23. Chou, S.-L. and W.-T. Tsai, *Effect of grain size on the hydrogen-assisted cracking in duplex stainless steels.* Materials Science and Engineering: A, 1999. **270**(2): p. 219-224.

24. Luu, W., P. Liu, and J. Wu, *Hydrogen transport and degradation of a commercial duplex stainless steel.* Corrosion science, 2002. **44**(8): p. 1783-1791.
25. An, X. and A. Dobson, *An influence of cathodic protection potential on the mechanical properties of super duplex stainless steel tube.* CORROSION 2009, 2009.
26. Chang, W., et al., *Effect of Cathodic Polarization Potential on Hydrogen Induced Stress Cracking of Duplex Stainless Steel.* CORROSION 2013, 2013.
27. Zakroczymski, T., A. Glowacka, and W. Swiatnicki, *Effect of hydrogen concentration on the embrittlement of a duplex stainless steel.* Corrosion science, 2005. **47**(6): p. 1403-1414.
28. Francis, R., G. Byrne, and G. Warburton, *Effects of cathodic protection on duplex stainless steels in seawater.* Corrosion, 1997. **53**(3): p. 234-240.
29. Kivisakk, U.H. and A.M. Holmquist, *Influence of Cathodic Protection on Hydrogen Embrittlement on Annealed and Cold Worked Duplex Stainless Steels.* CORROSION 2001, 2001.
30. Griffiths, A. and A. Turnbull, *Defining the limits of application of duplex stainless steel coupled to carbon steel in oilfield environments.* Corrosion, 2001. **57**(2): p. 165-174.
31. Hsu, J., S. Tsai, and H. Shih, *Hydrogen embrittlement of SAF 2205 duplex stainless steel.* Corrosion, 2002. **58**(10): p. 858-862.
32. Taylor, T., T. Pendlington, and R. Bird. *Foinaven Super Duplex Materials Cracking Investigation*. in *Offshore Technology Conference*. 1999.
33. Kivisäkk, U., *Relation of room temperature creep and microhardness to microstructure and HISC.* Materials Science and Engineering: A, 2010. **527**(29): p. 7684-7688.
34. Ronneteg, S., A. Juhlin, and U. Kivisäkk, *Hydrogen Embrittlement Of Duplex Stainless Steels Testing Of Different Product Forms At Low Temperature.* CORROSION 2007, 2007.
35. http://www.gamry.com/products/accessories/reference-electrodes/. 29.05.2014 [cited 2014 29.05.2014].

List of symbols

C_i	Surface concentration
C_0	Initial concentration
C(x,t)	Concentration at position x and time t
D	Diffusion coefficient
D_{eff}	Effective diffusion coefficient, including traps
D_0	Material specific maximum diffusion coefficient
E_A	Activation energy
E_L	Lattice binding energy
E_T	Traps binding energy
ΔE_x	Energy differences between normal lattice site and trap site
E’	Part of energy barrier related to trap sites
J	Diffusion flux
N_L	Number of lattice sites for hydrogen
N_T	Number of traps sites for hydrogen
R	Gas constant

Appendix A

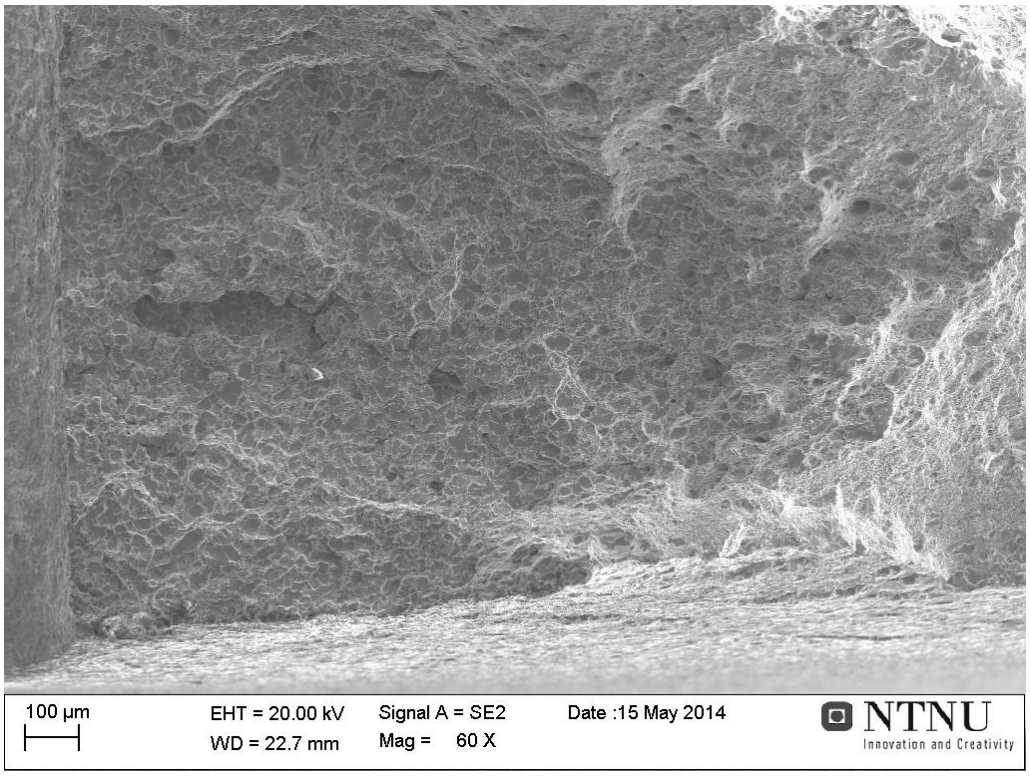

Figure 42 Lower left corner of the notched -1050mV$_{Ag/AgCl}$ sample

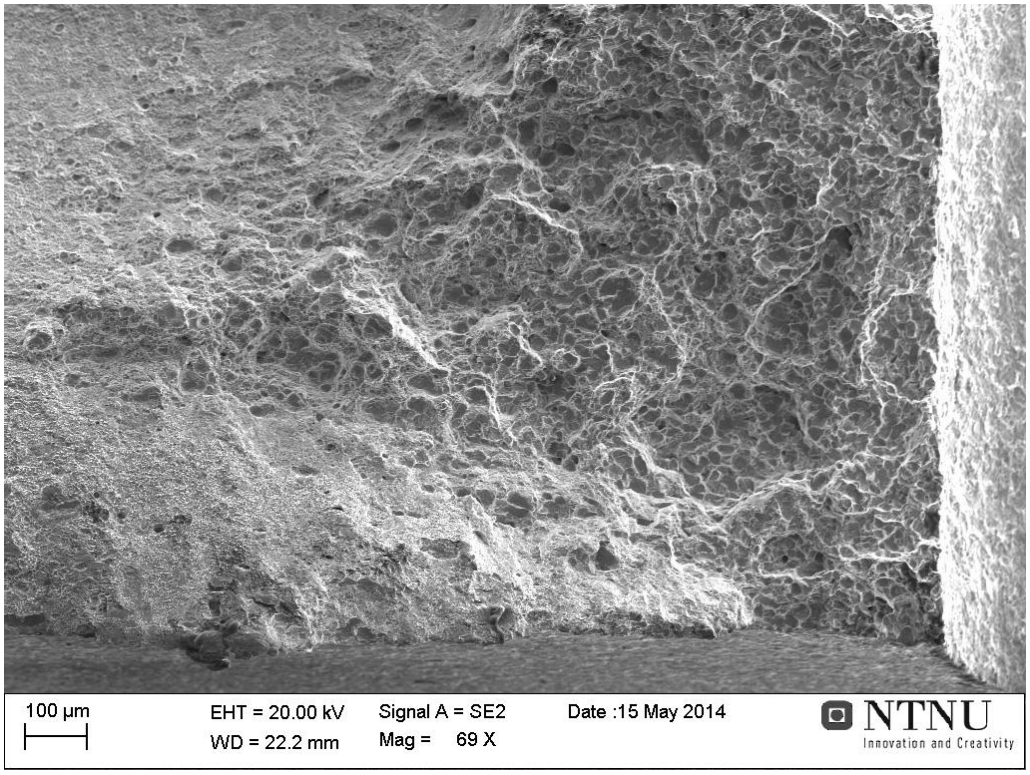

Figure 43 Lower right corner of the notched -1000mV$_{Ag/AgCl}$ sample.

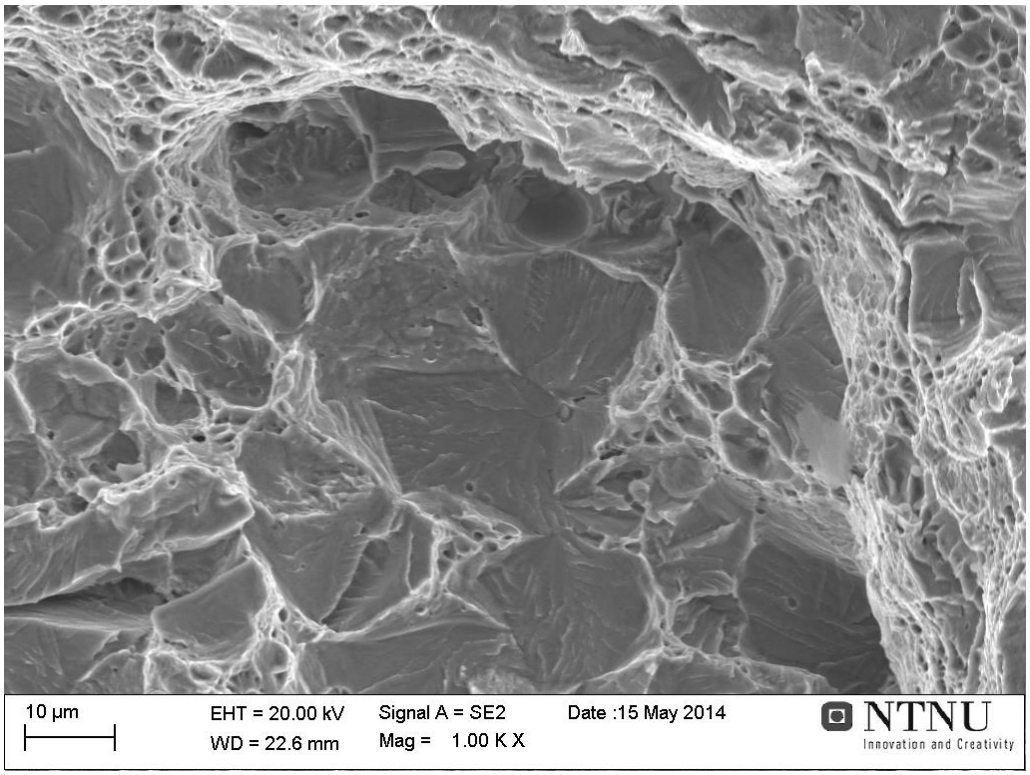

Figure 44 Higher magnification picture of the lower right corner of the -1000mV$_{Ag/AgCl}$ sample.

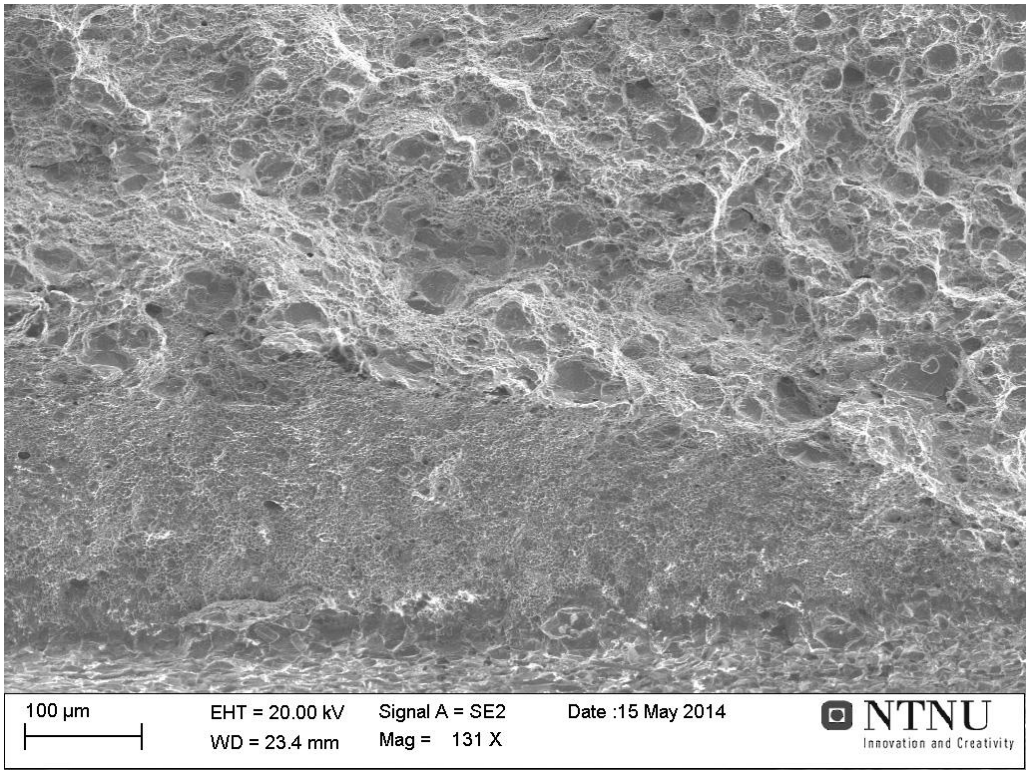

Figure 45 Centre of the -950mV$_{Ag/AgCl}$ sample.

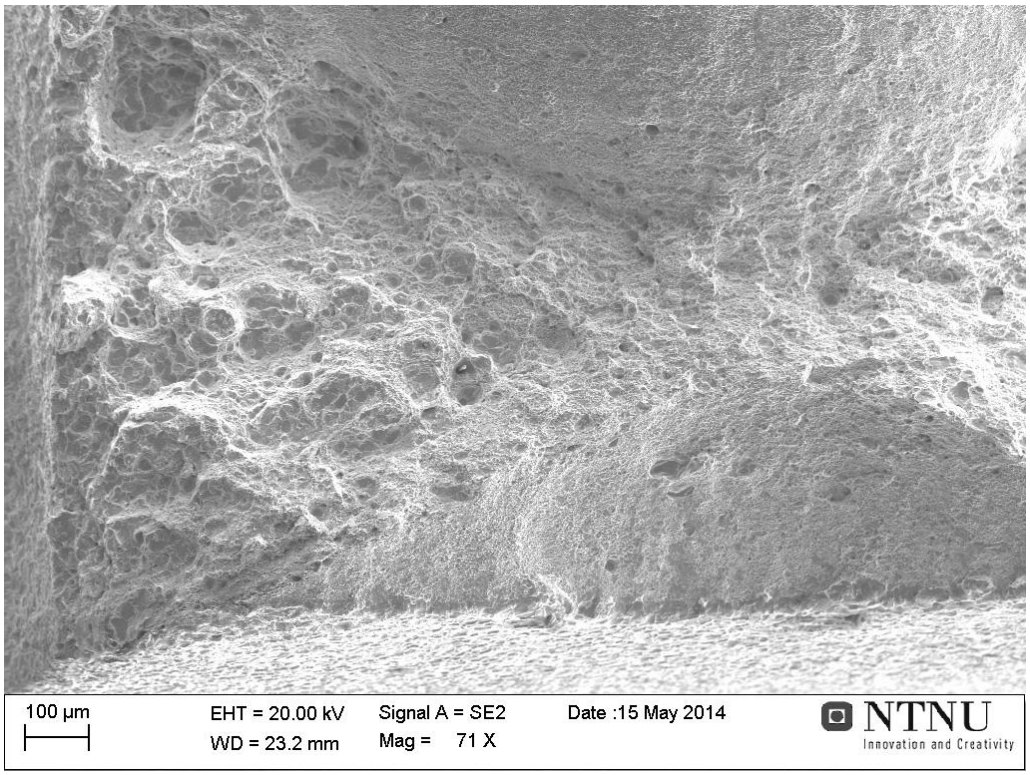

Figure 46 Lower left corner of the -900mV$_{Ag/AgCl}$ sample.

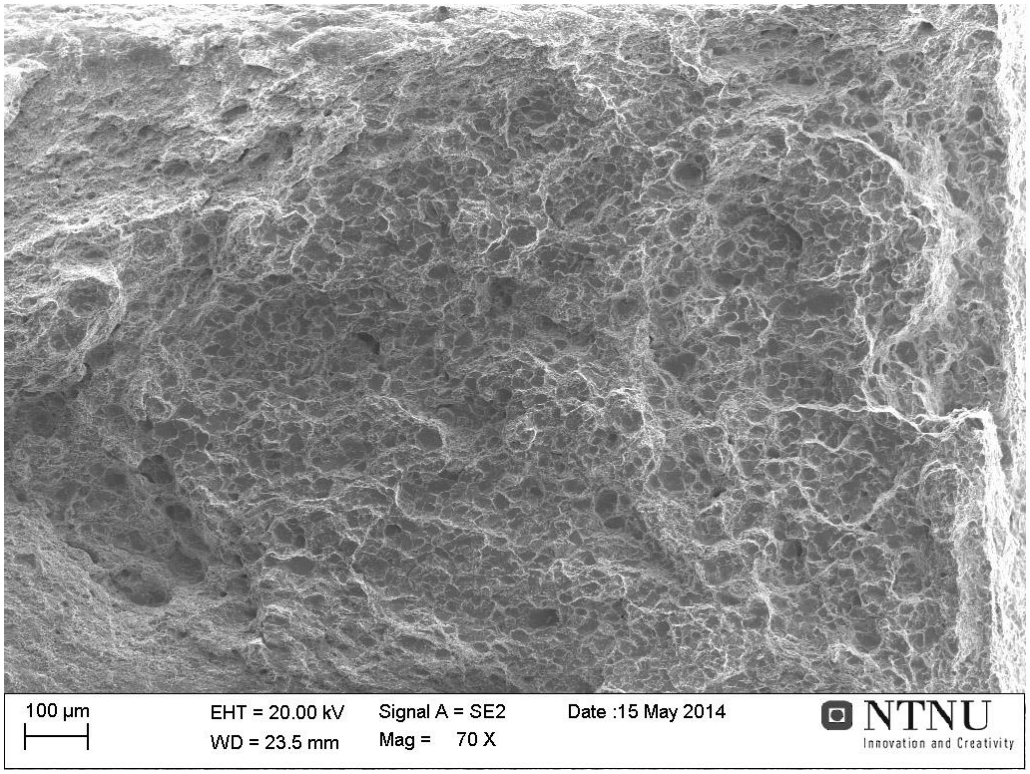

Figure 47 Right part of the -900mV$_{Ag/AgCl}$ sample.

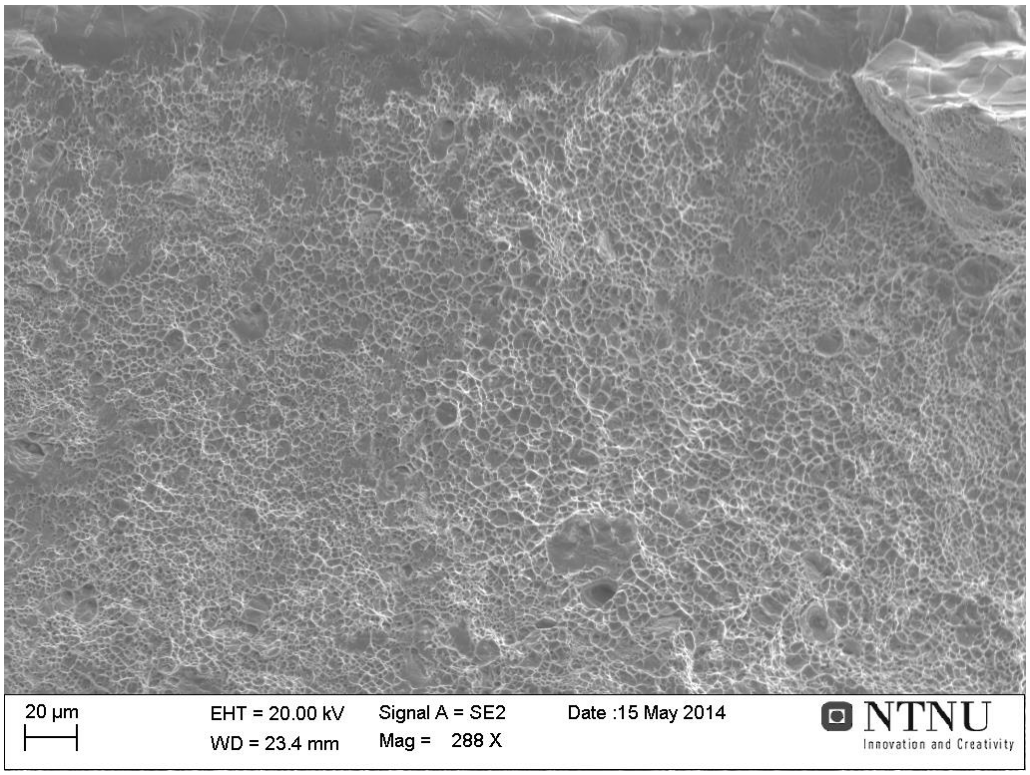

Figure 48 Upper centre part of the -800mV$_{Ag/AgCl}$ sample.

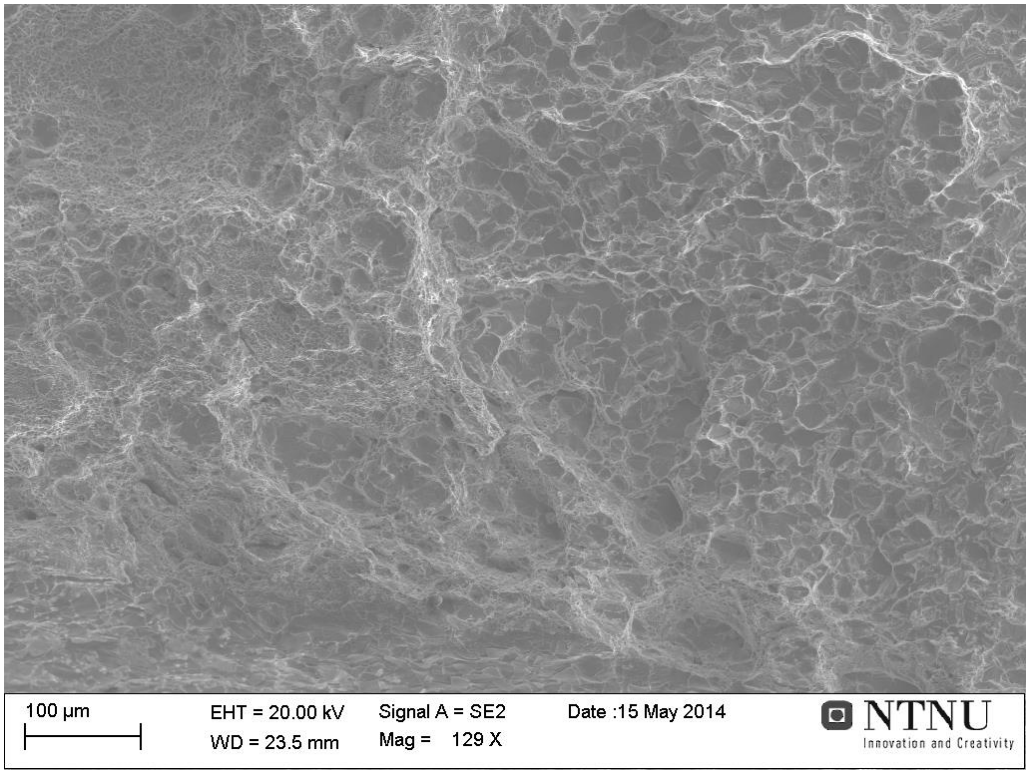

Figure 49 Lower right corner of the -800mV$_{Ag/AgCl}$ sample.

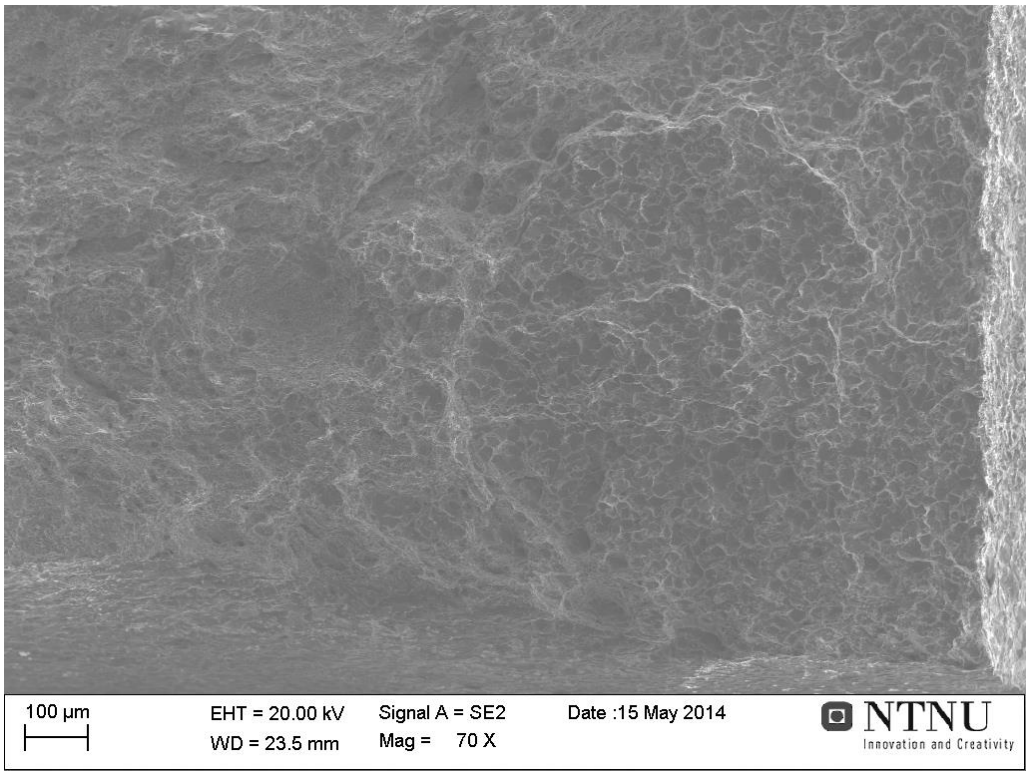

Figure 50 Lower right corner of the -800mV$_{Ag/AgCl}$ sample.

Appendix B

MatLab script used to make concentration profiles.

```
%Thick plate solution of Fick's 2nd law. Used to illustrate
concentration-
%profile for SDSS
clear all
Ci = 0; %ppm
C0 = 30; %ppm
t = 5*24*60*60; %s
D1 = 1.8*10^-6; %mm^2/s
D2 = 3.6*10^-8; %mm^2/s

T = 120 + 273; %K
R = 8.314; %J/K*mol
x = 0:0.001:0.8; %mm


for i = 1:length(x)
    C(i) = C0*(1 - erf((x(i))/((2*sqrt(D1*t)))));
    C2(i) = C0*(1 - erf((x(i))/((2*sqrt(D2*t)))));
end


plot(x,C,'r',x,C2,'b');
axis([0,0.800,0,C0])
xlabel('mm','FontSize',20)
ylabel('C [ppm]','FontSize',20)
title('Concentration profile / pre-charge','FontSize',20)
legend('D = 1.8*10^-^1^2 m^2/s','D = 3.6*10^-^1^4
m^2/s','Location','NorthEast')
```